An open-source hardware and software system for acquisition and real-time processing of electrophysiology during high field MRI

Patrick L. Purdon [a,*], Hernan Millan [b], Peter L. Fuller [c], Giorgio Bonmassar [b]

[a] Neuroscience Statistics Research Laboratory, Department of Anesthesia and Critical Care, Massachusetts General Hospital, 149 13th Street, Room 4005, Charlestown, MA 02129, United States
[b] MGH/MIT/HMS Athinoula A. Martinos Center for Biomedical Imaging, 149 13th Street, Charlestown, MA 02129, United States
[c] PLF Consulting, 258 Harvard Street #324, Brookline, MA 02446-2904, United States

ARTICLE INFO

ABSTRACT

Simultaneous recording of electrophysiology and functional magnetic resonance imaging (fMRI) is a technique of growing importance in neuroscience. Rapidly evolving clinical and scientific requirements have created a need for hardware and software that can be customized for specific applications. Hardware may require customization to enable a variety of recording types (e.g., electroencephalogram, local field potentials, or multi-unit activity) while meeting the stringent and costly requirements of MRI safety and compatibility. Real-time signal processing tools are an enabling technology for studies of learning, attention, sleep, epilepsy, neurofeedback, and neuropharmacology, yet real-time signal processing tools are difficult to develop. We describe an open-source system for simultaneous electrophysiology and fMRI featuring low-noise (<0.6 μV p–p input noise), electromagnetic compatibility for MRI (tested up to 7 T), and user-programmable real-time signal processing. The hardware distribution provides the complete specifications required to build an MRI-compatible electrophysiological data acquisition system, including circuit schematics, print circuit board (PCB) layouts, Gerber files for PCB fabrication and robotic assembly, a bill of materials with part numbers, data sheets, and vendor information, and test procedures. The software facilitates rapid implementation of real-time signal processing algorithms. This system has been used in human EEG/fMRI studies at 3 and 7 T examining the auditory system, visual system, sleep physiology, and anesthesia, as well as in intracranial electrophysiological studies of the non-human primate visual system during 3 T fMRI, and in human hyperbaric physiology studies at depths of up to 300 feet below sea level.

Published by Elsevier B.V.

1. Introduction

Simultaneous recording of electrophysiology during functional magnetic resonance imaging (fMRI) is a technique of increasing importance in brain imaging research. Commercial solutions exist for data acquisition and analysis of these data, but with the rapid development of new neuroscience and clinical applications, there is a growing need for end-user customization of both hardware and software for data acquisition and real-time processing. In many studies, hardware customization may be necessary to meet application-specific requirements for acquisition bandwidth, number of channels, amplifier configurations, and other hardware design specifications. Software customization is also an important feature for many applications, particularly for those that require real-time processing of acquired data. For studies examining epilepsy, sleep, or drug effects, for example, the ability to observe the study subject's electrophysiological state in real-time is essential for success (e.g., epileptic spiking activity, sleep stage, etc.) (Lemieux et al., 2001; Portas et al., 2000; Schomer et al., 2000). Such real-time observations would allow the investigator to be certain that an adequate amount of data are being recorded in each desired electrophysiological state during an experiment. ERP studies conducted simultaneously with fMRI would benefit in a similar way from real-time processing, since the duration of a scan could be adjusted to ensure that an adequate number of trials were observed. Real-time processing is also required for biofeedback studies, where study subjects must be able to observe, with minimal delay, their own electrophysiological state to permit feedback control (Basmajian, 1981; Delorme and Makeig, 2003; Fox, 1979; Herrmann et al., 2004; Hill and Raab, 2005; Riddle and Baker, 2005; Sinkjaer et al., 2003).

Instrument design for electrophysiological recording during MRI is difficult due to the presence of the large static and gradient magnetic fields, and radiofrequency fields, each of which introduces

---

* Corresponding author. Tel.: +1 617 724 1060; fax: +1 617 726 8410.
E-mail address: patrickp@nmr.mgh.harvard.edu (P.L. Purdon).

Table 1
MRI Safety: Potential adverse interactions between a MRI environment and a medical device

Imaging field	Physical effect	Potential complications
Static magnetic field	Eddy currents Acceleration due to magnetic force Electrodes perturb field homogeneity	Tearing of tissues during patient insertion Serious injuries or death due to "missile effect" Image artifact and/or distortion
Gradient magnetic field	Faraday's induced currents (dB/dt)	Painful peripheral nerve stimulation Device malfunction or failure
Radio frequency field	RF power deposition on tissues Device induced EM interference Leads perturb RF field	Excess tissue heating or burns Noise in MR images Poor image SNR

potential complications for safety, instrument function, and image quality (United States Food and Drug Administration, 1997; Huang-Hellinger et al., 1995; Ives et al., 1993; Lemieux et al., 1997; Chen, 2001; Bonmassar et al., 2001; Angelone et al., 2004, 2006; Vasios et al., 2006). These complications are summarized in Table 1. Hard-to-find non-ferromagnetic components must be used throughout the design to minimize complications from the static magnetic field. Print circuit boards (PCBs) must be designed to minimize pickup of gradient artifacts and transmission of RF interference, and electrodes and electrode leads must be made with special materials to prevent RF heating and minimize susceptibility artifacts (Vasios et al., 2006). A number of strategies exist for removing the magnetic gradient artifact, ranging from subtraction of a template waveform (Allen et al., 2000; Niazy et al., 2005) to synchronization of the electrophysiological sampling with gradient switching (Goldman et al., 2000; Anami et al., 2003; Mandelkow et al., 2006). In all cases, the dynamic range of the instrument must be large enough to record the gradient artifact without saturation or distortion. Ballistocardiogram artifacts, EEG artifacts induced by cardiopusatile motion within the static magnetic field, remain a problem, and can be removed with post-processing methods (Allen et al., 1998; Bonmassar et al., 2002; Niazy et al., 2005) or reduced in amplitude by using specially designed EEG electrodes (Vasios et al., 2006) or head restraint methods (Anami et al., 2003). Table 2 summarizes additional performance characteristics that are needed for electrophysiological recording within the MRI environment. Development of data acquisition and real-time processing software is also challenging, since the software must interact at a low-level with hardware and hardware drivers, and work quickly enough to keep up with acquired data, while maintaining high-level functionality for ease of use and customization.

One way to facilitate hardware and software customization and development would be to make the hardware and software freely available in an open-source fashion. For software, the open-source model has been extremely successful by facilitating collaboration between large groups of researchers and developers, with few requirements for success beyond a computer and programming knowledge. With hardware, the analogous open-source concept is more challenging. While it is easy to distribute and modify circuit schematics, if the hardware are sufficiently complex, the ability to reduce the design to practice, through multiple design and construction steps (circuit, PCB, components, etc.) becomes a limiting factor. Ongoing developments in electronics construction technology, such as 3D printers and circuit printers, are reducing these limitations by allowing automated construction of electronic circuits and systems based on construction files (e.g., Gerber files, robotic assembly files) that fully specify the system (Chalamala and Temple, 2005; Mei et al., 2005; Mikhak et al., 2002). To make open-source hardware reducible to practice in the way that open-source software is, open-source hardware would need to include not only schematics for the circuit designs, but also an integrated library of construction files that would allow end-users to construct the hardware using largely automated methods, and a means to compile these files in an organized way with successive design changes.

In this paper we describe an open-source hardware and software system for acquisition and real-time processing of electrophysiology during high-field MRI (up to 7 T). We have named this system "High Field One" (HF-1). A novel aspect of this work is that all elements of the system have been gathered together into a comprehensive, freely available open-source distribution. The hardware has been designed to minimize electromagnetic interference (EMI) between the data acquisition device and the MRI, and features EMI-reducing PCB designs, double shielding, and low input noise. The hardware distribution includes all circuit and PCB design files, a bill of materials and data sheets for all components, including difficult to find non-ferrous connectors and parts, construction files for automated assembly, and test procedures, compiled together to promote rapid and organized development. The software distribution includes data acquisition software from high-level LabView virtual instruments (VIs) down to low-level firmware, as well as high-level real-time processing functions implemented in LabView. This open-source system will allow end-users to build an MRI-compatible electrophysiological acquisition system, with the ability to modify the design to their individual specifications, and to

Table 2
Specifications for recording electrophysiology during MRI

	MRI standard	Specification in HF-1
Field strength	1.5 T	7 T
DAC resolution	16 bits	24 bits
Input signal range	±20 to 30 mV	−176 to +174 mV
LSB resolution	0.30–0.46 μV nominal	0.024 μV nominal
Scanner synchronization	NO	YES
External clock	NO	YES
Real-time processing	NO	YES
End-user customization	NO	Open-source hardware and software
Bandwidth	0.1–70 Hz	DC to 4 kHz
Shielding	Faraday shield	Double-shielding
Electrode heating protection	15 kΩ discrete resistors	Ink Cap (resistive leads reduce SAR)
Electrode artifacts	AgCl electrodes	Ink Cap (AgCl ink reduces susceptibility artifacts)

develop custom data acquisition and real-time processing applications. The HF-1 software and hardware designs are freely available at http://www.nmr.mgh.harvard.edu/abilab. Users must agree to a free licensing agreement prior to software and hardware design download, in accordance with Harvard Medical School and Massachusetts General Hospital policies.

This manuscript is organized into five main sections: (1) Introduction, (2) Materials and Methods, (3) Results, (4) Discussion, and (5) Conclusions. Principles of design for instruments used in the MRI are discussed in Section 1. In Sections 2.1 and 2.2 we provide an overview of the hardware and software design, as well as their open-source dissemination. In Section 2.3, we describe data recording and real-time processing examples, with results of these examples presented in Section 3, In Section 4 we discuss other applications and future work. Table A.1 provides a list of acronyms used in this paper.

2. Materials and methods

The HF-1 system is organized into a number of hardware and software subsystems. The hardware is organized into eight main subsystems (Fig. 1): (1) an external amplifier unit, (2) an anti-aliasing and level shifting stage, (3) an analog-to-digital conversion (ADC) stage, (4) a programmable microcontroller unit (MCU) for controlling ADC functions, (5) an optical communications unit for acquisition control and data transfer based on the universal serial bus (optical USB), (6) a computer for data display, recording, integration with external signals such as event triggers and physiological monitoring, and real-time signal processing, (7) an optional external buffer unit to interface with high impedance electrodes, and (8) an optional electrode adapter unit for use of individual EEG electrodes during non-MRI studies. The software system is organized into four main subsystems (Fig. 2): (1) microcontroller (MCU) code for low-level data acquisition control, (2) high-level graphically based data acquisition software written in LabView (National Instruments, Austin, TX), (3) high-level real-time processing modules written in LabView, and (4) Matlab-based post-processing utilities (Mathworks, Natick, MA). HF-1 is compatible with MRI at field strengths of up to 7 T, and can be used for both EEG and more general electrophysiological recordings such as local field potential (LFP) or multi-unit activity (MUA) using the external buffer unit for high impedance electrodes. In this section we provide a brief overview of hardware and software design.

2.1. Hardware overview

The main features of the HF-1 hardware system are:

1. Variable sampling rate of up to 20 kHz per channel.
2. Bandwidth from DC to one of two hardware-specified values (default 300 Hz or 4 kHz).
3. High dynamic range achieved through use of 24-bit analog-to-digital converters (ADC).
4. Low input noise (<1 μV peak-to-peak).
5. Programmable microcontroller unit (MCU) to permit end-user customization of data acquisition functions.
6. Option to synchronize between electrophysiological acquisition and MRI acquisition clock to improve gradient artifact removal.
7. Tested at MRI field strengths of up to 7 T.
8. Optical USB communications unit for simple and reliable digital data transfer to acquisition computers.
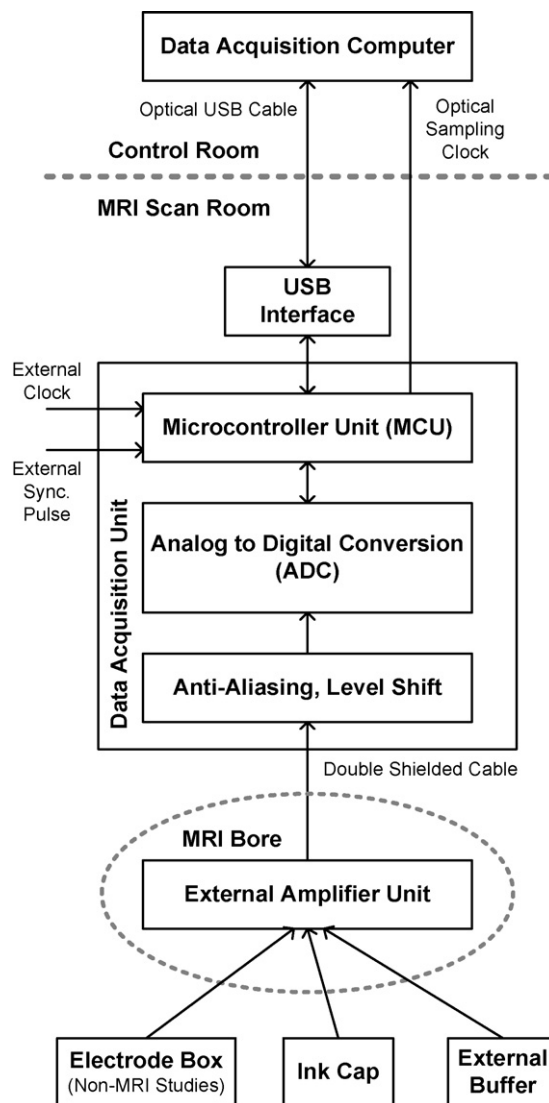

Fig. 1. High-field-1 (HF-1) hardware overview, showing a schematic representation (left) and labeled photos of the subsystems (right).
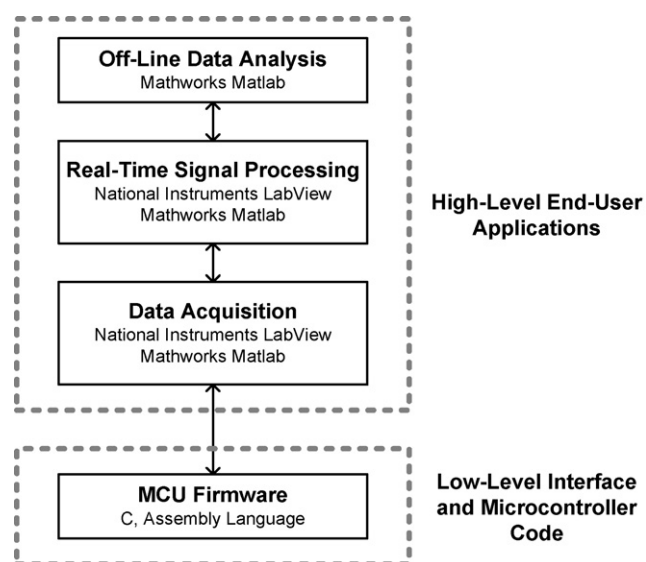

Fig. 2. High-field-1 (HF-1) software overview.

Tables 2 and 3 provide a summary of HF-1's technical specifications. The system (Fig. 1) is typically connected to an MRI-compatible electrodes designed to prevent RF-related heating using distributed resistance leads ("Ink Cap") (Angelone et al., 2004; Vasios et al., 2006). Amplification is performed by an external amplifier unit, while anti-aliasing filtering, level shifting, and analog-to-digital conversions are performed by the data acquisition unit. The data acquisition unit is non-ferromagnetic and can be placed inside the bore, but is usually placed outside the bore to reduce pickup of magnetic gradient artifacts. The digitally sampled electrophysiological data are buffered, packaged into discrete "data packets" (described below), and then transferred via optical USB. The system is powered by two 12-V lead acid batteries, and in this way is isolated from electrical mains.

The HF-1 hardware has been carefully designed to minimize hardware interactions with the static magnetic, gradient magnetic, and radiofrequency fields (see Table 1). All components in HF-1 are non-ferromagnetic, and are fully specified with part numbers and vendors in the open-source distribution bill of materials (described in Section 2.2.4). These non-ferromagnetic components include aerospace-grade connectors made from non-ferrous stainless steel, chassis constructed from plastic, aluminum, and copper, and integrated circuits (ICs) that have been screened for ferromagnetism using high-field neodymium magnets and the MRI static field itself. Magnetic screening of ICs is required because the metallurgy of ICs is rarely specified in the data sheets. Interactions with the gradient magnetic field are controlled by minimizing the size of loops formed on PCB traces. Radiofrequency (RF) interference is controlled in three ways: (1) PCB layouts designed to minimize RF emissions and reception, (2) double-shielding on cables and chassis, and (3) capacitive filter connectors to minimize RF emissions through apertures in the shielded chassis.

The first-stage amplifier uses the Analog Devices AD620B instrumentation amplifier (Analog Devices, Norwood, MA). The AD620B features low gain nonlinearity (10 ppm), high bandwidth (120 kHz with gain of 100), and wide power supply range ($V_S = \pm 18$ V) and output range (within 1.2 V of V_S) to accommodate the potentially large gradient artifacts encountered in electrophysiological recordings taken during MRI (Analog, 2004). The gain (G) on the external amplifier unit is set during board construction depending on the dynamic range required. In situations where background noise levels are high, due to the helium pump, high slew-rate gradients, or when conventional EEG caps are used, the gain is set to $G = 50$ to provide a wide input range of input range of -176 to $+174$ mV. If

Table 3
Technical specifications for HF-1

Analog input and ADC	
Number of channels	32
Input noise	0.6 μV p–p (at $G = 500$); 6 μV p–p (at $G = 50$)
Input configuration	Referential or unbalanced differential (with adaptor)
ADC bit resolution	24 bits nominal, 19 effective
Input signal range	-17.6 to $+17.4$ mV (at $G = 500$); -176 to $+174$ mV (at $G = 50$)
Resolution	0.024 μV nominal, 0.67 μV effective
Type of ADC	Delta–sigma
Sampling rates (fs)	978 or 20,833 Hz
Data transfers	USB 1.1
Input impedance (ground referenced)	1 MΩ ∥ 3 nF
Level-shift anti-aliasing filter	DC to 300 Hz (at fs = 978 Hz) or 4 kHz (at fs = 20.833 kHz)
ADC anti-aliasing filter	DC to 4.24 kHz
Power supply rejection ratio (PSRR)	90 dB at 60 Hz
Common-mode rejection ratio (CMRR)	100 dB at 60 Hz
Triggers (from NI USB-6210)	
Analog trigger	
Number of triggers available	8
Input range	± 10, 5, 1 and 0.2 V
Resolution	16 bits
Digital trigger	
Compatibility	5 V TTL/CMOS
Response	Rising or falling edge
Pulse width	10 ns minimum
Connectors	
Analog signal input	37-pin Micro-D (pin)
Analog trigger input	BNC (Socket)
Digital trigger input	BNC (Socket)
External synchronization pulse input	SMA (Socket)
External clock input	SMA (Socket)
Sampling clock output	Versatile link plastic connector (fiber optic; Avago Technologies, San Jose, CA)
Digital signal output	USB (Type A, Plug)
Electrical characteristics	
Isolation	Battery operated
Battery 1	12 V 33 Ah lead acid (max 800 mA power consumption)
Battery 2	12 V 17 Ah lead acid (max 60 mA power consumption)
Input overload protection	15 V, 60 mA (over several hours)
Physical characteristics	
Dimensions	$10 \times 10 \times 4''$
Weight	7 lbs
Operating temperature	Nominal
Tested operating depth	300 fsw

background noise levels are lower, for instance when using EEG caps with resistive leads to reduce RF and gradient noise coupling (Vasios et al., 2006), a higher gain setting of $G = 500$ is used, providing an input range of -17.6 to $+17.4$ mV.

ADC functions are performed by the Texas Instruments ADS1254E, a low-power, low-noise, high-speed ADC whose 24-bit resolution provides the high dynamic range required for electrophysiological recordings during MRI (Texas instruments, Dallas, TX). Each ADS1254 chip has four differential inputs, which can be multiplexed at a rate of up to 1 kHz per channel (Instruments, 2001). Alternatively, a single channel can be sampled at up to 20 kHz. To provide 32 acquisition channels, an architecture using 8 ADS1254's was chosen, each running with 4-channel multiplexing at 1 kHz. If a higher-rate sampling is required, a single channel from each ADS1254 can be sampled, giving 8 channels at 20 kHz per channel. The sampling scheme can be selected at a high-level in the LabView data acquisition software, or at a low-level by interacting directly with the MCU. The analog input to each ADS1254 is first anti-alias filtered and then re-scaled to a 0–5 V dynamic range using an op-amp-based scaling and level-shift circuit (Instruments, 2001). Anti-aliasing filtering is achieved using a one-pole lowpass RC divider with software-selectable cutoff frequency, yielding a bandwidth of DC to either 300 Hz or 4 kHz. The selection is performed by a MCU-controlled transistor switch that controls the capacitance of the RC circuit, and can be controlled with HF-1's LabView data acquisition software. If necessary, these cutoff frequencies can be adjusted during board construction by changing the component values of the RC divider. In addition, the ADS1254 has its own anti-aliasing filter from DC to 4.24 kHz.

The ADS1254 provides a 19.1-bit RMS effective resolution due to inherent noise within the integrated circuit, which provides an effective resolution of 0.71 μV in the least significant bit (LSB) when the gain is set to $G = 50$, and an effective resolution of 0.071 μV LSB when the gain is set to $G = 500$. Noise measurements were performed in a shielded room (Braden Shielding Systems, Tulsa, OK) with all amplifier inputs short circuited to ground, yielding a peak-to-peak noise of 6 μV when the gain is set to $G = 50$, and a peak-to-peak noise of 0.6 μV when the gain is set to $G = 500$. For the recordings described in Sections 2.3 and 3, a gain of $G = 50$ was used.

Signal-to-noise within the MRI scanner is improved by placing the external amplifier unit close to the study subject and electrodes, allowing the signal to be amplified before MRI-related noise sources can be picked up. These noise sources come primarily from the gradient and static magnetic fields (e.g., gradient switching, vibrations from helium pump). To minimize noise coupling from these sources, several measures are taken. The chassis and cabling are all double-shielded to reduce RF noise coupling. The external amplifier unit has been designed with a compact circuit layout that reduces gradient and static magnetic noise pickup. The USB and ADC subsystems, which tend to have larger circuit boards due to their higher level of complexity, are located outside the MRI bore to further reduce magnetic noise coupling.

Data are transmitted via optical USB interface to a computer located outside the MRI scanner room. Auxiliary input signals such as event triggers or additional analog signals are integrated with the main electrophysiological data using a National Instruments NI USB-6210 multifunction data acquisition unit (National Instruments, Austin, TX). Data acquired on the NI USB-6210 are synchronized with the main electrophysiological acquisition by a sampling clock sent from the HF-1 data acquisition unit via optical link (Versatile Optical Link, Avago Technologies, Palo Alto, CA). The HF-1 data acquisition unit can also receive external synchronization signals (Fig. 1). One signal synchronizes data acquisition with the MRI scanner's TR or trigger pulse, a TTL pulse that signals the start of

each volume acquisition in fMRI. The other external synchronization signal substitutes the onboard 48 MHz system clock with an external 48 MHz clock generated by a direct digital synthesis (DDS) device driven by the MRI Scanner's 10 MHz clock.

2.2. Software overview

The main subsystems of the HF-1 software are:

1. Microcontroller (MCU) firmware for low-level data acquisition control.
2. Data acquisition software written in LabView (National Instruments, Austin, TX).
3. Real-time processing modules written in LabView.
4. Matlab-based post-processing utilities.

These software subsystems are open source, and are documented and organized to facilitate end-user customization and further development.

2.2.1. MCU firmware and data packet specification

The MCU firmware provides low-level control of data acquisition functions such as reading data from the ADCs, assembling the data into packets, and then placing these data packets into a buffer for transfer by the optical USB unit. The firmware was written in C and assembler, and was structured to facilitate customization as well as porting to other programming languages as newer or more powerful MCU hardware become available. The typical HF-1 user would not have to interact directly with the MCU firmware, as most functions can be controlled from the high level LabView data acquisition and real-time processing software (discussed below). However, this remains an option for more advanced applications and hardware modifications.

The data packet format is shown in Fig. 3. Each data packet begins with an 11-byte header that identifies the beginning of every packet, indicates the system status, and specifies the data size. The first 8 bytes of the header contain a fixed pre-set sequence that is used to identify the beginning of a packet. The next byte ("status byte") indicates the channel number and sampling routine (either sampling from a single channel on each ADC or "rotating" through all four channels in succession), as well as the value chosen for the anti-aliasing filter (either 300 Hz or 4 kHz). The remaining 2 bytes specify the data set size. The raw data are transmitted after the header. When sampling from a single channel on each ADC at 20 kHz, a maximum of 16 data frames can be transmitted per packet, with 8-channels per frame. When sampling from all four channels on each ADC at 1 kHz per channel, a maximum of 4 data frames can be transmitted per packet, with 32-channels per frame. The data packet is designed to send data sets of any size, so data sets are divided into several data packets, with the remainder of data awaiting transfer indicated in the last two bytes of the header ("data set size"). Given the 11 bytes header, 373 of the 384 bytes in each packet contain data, yielding an overhead of 2.9%. Data packet parsing is handled automatically within the included LabView data acquisition software.

2.2.2. LabView data acquisition and real-time processing software

The HF-1 data acquisition and real-time processing software were written using the National Instruments LabView 8.2 programming language (National Instruments, Austin, TX) under Microsoft Windows (Microsoft, Richmond, WA). LabView is a high-level graphical programming language that facilitates rapid development of data acquisition and real-time processing applications through its intuitive graphical programming language and its wide

Data Packet Format, 8-channel 20 kHz Mode:

Byte #	Type	Value	Channels	Frame #
1	Header: Start of data packet	0xFE		
2	Header: Start of data packet	0xDC		
3	Header: Start of data packet	0xBA		
4	Header: Start of data packet	0x98		
5	Header: Start of data packet	0x76		
6	Header: Start of data packet	0x54		
7	Header: Start of data packet	0x32		
8	Header: Start of data packet	0x10		
9	Header: Status	Acquisition Parameters		
10	Header: Lo data set length	Indicates remaining data		
11	Header: Hi data set length	Indicates remaining data		
12	Byte 1	Bits # 23	1-8	16
…	…	…	1-8	16
35	Byte 24	Bits # 0	1-8	16
…	…	…	…	…
361	Bytes 1	Bits # 23	1-8	1
…	…	…	1-8	1
384	Bytes 24	Bits # 0	1-8	1

Data Packet Format, 32-channel 1 kHz Mode:

Byte #	Type	Value	Channels	Frame #
1	Header: Start of data packet	0xFE		
2	Header: Start of data packet	0xDC		
3	Header: Start of data packet	0xBA		
4	Header: Start of data packet	0x98		
5	Header: Start of data packet	0x76		
6	Header: Start of data packet	0x54		
7	Header: Start of data packet	0x32		
8	Header: Start of data packet	0x10		
9	Header: Status	Acquisition Parameters		
10	Header: Lo data set length	Indicates remaining data		
11	Header: Hi data set length	Indicates remaining data		
12	Byte 1	Bits # 23, MSB	1-8	4
…	…	…	1-8	4
35	Byte 24	Bits # 0, LSB	1-8	4
36	Byte 1	Bits # 23, MSB	9-16	4
…	…	…	9-16	4
59	Byte 24	Bits # 0, LSB	9-16	4
60	Byte 1	Bits # 23, MSB	17-24	4
…	…	…	17-24	4
83	Byte 24	Bits # 0, LSB	17-24	4
83	Byte 1	Bits # 23, MSB	25-32	4
…	…	…	25-32	4
107	Byte 24	Bits # 0, LSB	25-32	4
…	…	…	…	…
289	Byte 1	Bits # 23, MSB	1-8	1
…	…	…	1-8	1
312	Byte 24	Bits # 0, LSB	1-8	1
313	Byte 1	Bits # 23, MSB	9-16	1
…	…	…	9-16	1
336	Byte 24	Bits # 0, LSB	9-16	1
337	Byte 1	Bits # 23, MSB	17-24	1
…	…	…	17-24	1
360	Byte 24	Bits # 0, LSB	17-24	1
361	Byte 1	Bits # 23, MSB	25-32	1
…	…	…	25-32	1
384	Byte 24	Bits # 0, LSB	25-32	1

Fig. 3. USB data packet example. The top panel shows the data packet format for 8-channel, 20 kHz mode, while the lower panel shows the data packet format for 32-channel, 978 Hz mode. The first 11 bytes of the data packet code a header, consisting of an 8-byte code denoting the start of the data packet, a *status* byte, and two *data set length* bytes. The data fills out the remainder of the packet.

assortment of built-in data acquisition, data display, and data analysis functions. Fig. 4 shows the top-level block diagram of the LabView code, annotated to illustrate the location of modules that control initialization, data acquisition from HF-1 via USB, data acquisition from external digital I/O lines (from the NI USB-6210), keyboard and display controls, and real-time processing. Fig. 5 shows the graphical user interface for the data acquisition as an example of real-time time-domain ERP averaging of visual evoked potentials, while Fig. 14 shows real-time frequency domain ERP averaging interface.
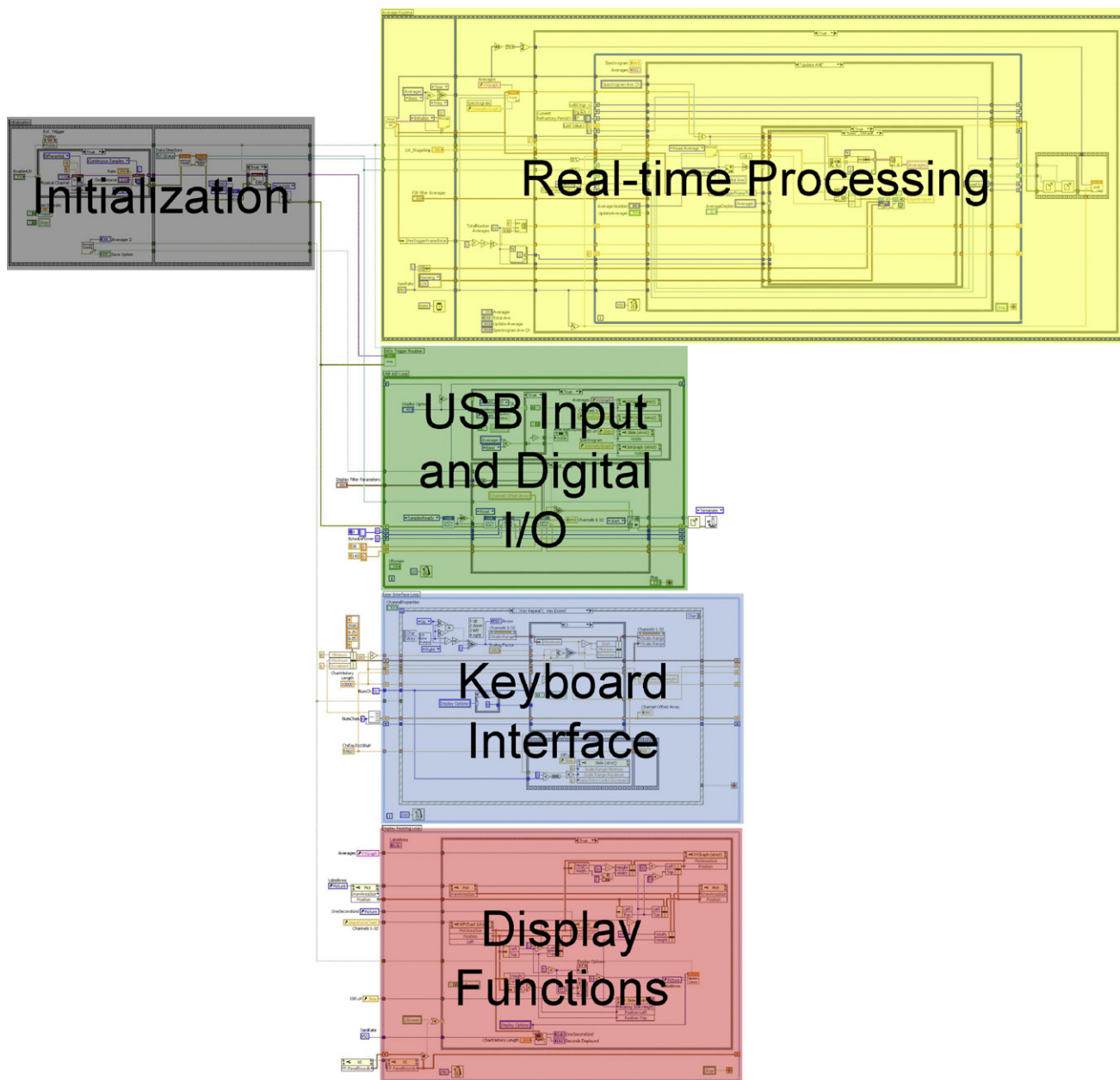
Fig. 4. Top-level block diagram of LabView data acquisition virtual instrument (VI), illustrating layout of initialization, real-time processing, digital I/O, USB input, keyboard interface, and display functions.

The real-time processing module operates on trigger-driven windows of data, with user configurable pre- and post-trigger data segments. Low-, high-, or bandpass filtering can be applied to the data prior to window selection and real-time processing, with filter settings that are independent of any filtering chosen for data display or data storage. The user is also able to specify separate amplitude rejection limits for each channel to improve the data quality entering into the real-time processing stream. The real-time module operates on all acquired channels simultaneously, but can also be configured to operate on subsets of channels if desired.

The data acquisition and real-time processing software run on Microsoft Windows XP Professional (version 5.1, service pack 2; Microsoft Corporation, Redmond, WA), on a Sony Vaio Laptop (VGN-FE590P; Sony USA, New York, NY) with 2 GHz Intel Core Duo T2500 central processing unit (CPU; Intel x86 Family 6 Model 14 Stepping 8; Intel Corporation, Santa Clara, CA) and 2 GB RAM.

Approximately 80% of the CPU's resources are utilized to run Lab-View 8.2 and the data acquisition and real-time software. For comparison, a low-level C program for acquiring the EEG data (without display or real-time processing) uses approximately 10% of the CPU's resources. Data acquisition from the USB interface utilizes a peak bandwidth of approximately 600 kilobytes/s, or 40% of the full speed USB 1.1 bandwidth.

2.2.3. Matlab-based post-processing utilities

The data recorded by the DAQ application are stored in three separate files: a *.dat file that holds the raw binary electrophysiological data, a *.trg file that stores the external trigger and external signal information, and a *.evn file that stores keyboard annotations, all with the same base filename (e.g., file.dat, file.trg, file.evn). This triplet of files can be read into Matlab using utility functions included with the HF-1 software distribution. Once in
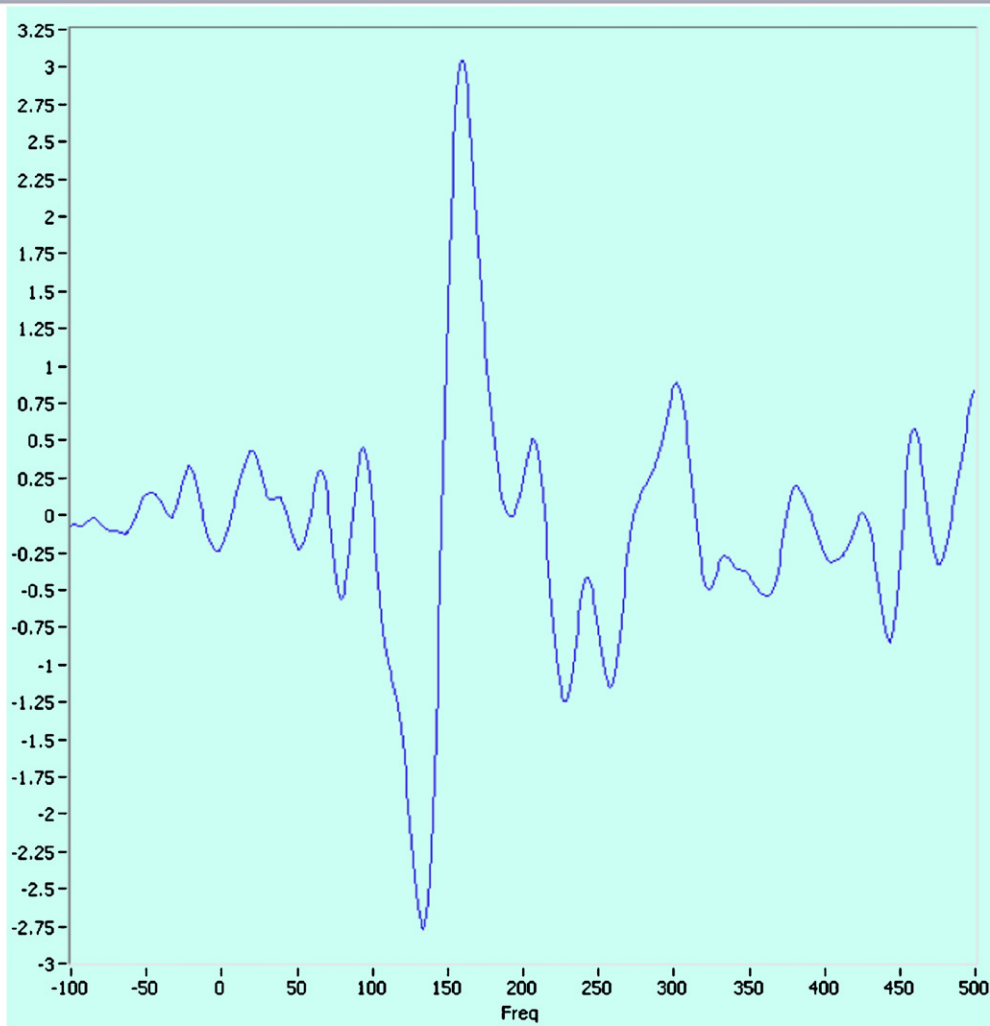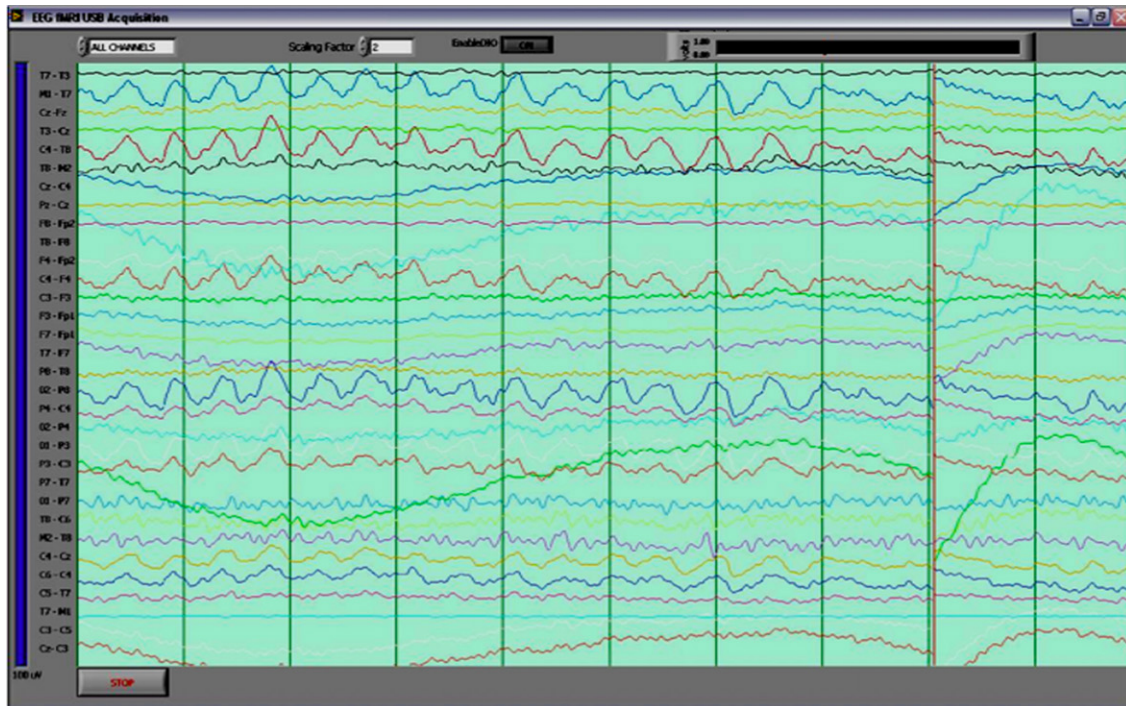
Fig. 5. Graphical user interface of LabView data acquisition program ("virtual instrument," VI), showing 32 traces of EEG (top) and an example of real-time time-domain averaging of VEPs in a human study subject (bottom).
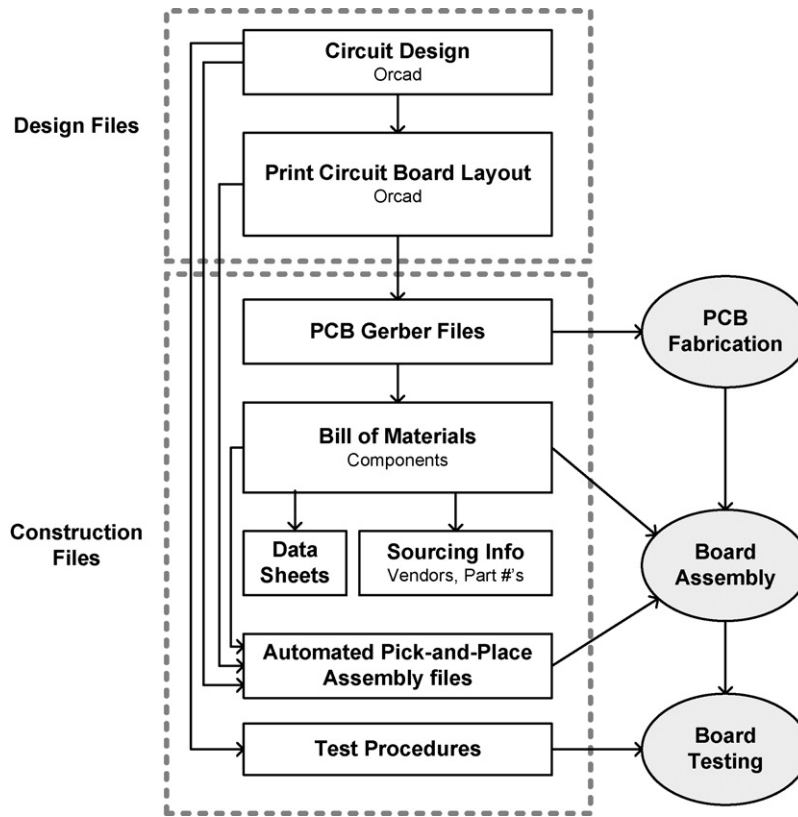
Fig. 6. Design and construction files for HF-1 hardware distribution, and their use in PCB fabrication, board assembly, and testing.

Table 4
Manufacturing requirements for building HF-1 hardware

Manufacturing step	Requirements
PCB fabrication	Eight layers, 5-mil traces, double-sided, 10 mil vias
Component sourcing	Must conform with all specifications (values, footprints) in bill of materials. Non-magnetic avionics grade chassis, cables, and connector components required
Automated pick-and-place assembly	Capable of pick-and-place assembly with hand-fed parts down to 0402 surface mount size, soldermask using laser cut stencil, convection reflow oven

Matlab, the data can be post-processed or converted to other file formats.

2.2.4. Software and hardware dissemination

The HF-1 software and hardware designs are freely available at http://www.nmr.mgh.harvard.edu/abilab. Users must agree to a free licensing agreement prior to software and hardware design download, in accordance with Harvard Medical School and Massachusetts General Hospital policies. The software is compatible with LabView 8.2 or later (National Instruments, Austin, TX), under a Microsoft Windows XP operating system (Microsoft, Richmond, WA). The hardware distribution is summarized in Fig. 6. The hardware design, including both circuit schematics and print circuit board (PCB) layout, are provided in Orcad format. Detailed hardware construction files are also provided to help the end-user build a complete system. Gerber files are provided for PCB construction. The bill of materials (BOM) specifies all required components, along with component specifications, data sheets, and sourcing information such as vendors and part numbers. Files to drive automated pick-and-place circuit board population and assembly are also included, as well as test procedures for each of the HF-1 circuit boards. With these construction files, most of the system can be built in a largely automated fashion. Manufacturing require-

ments for each of the HF-1 sub-assemblies is listed in Table 4. At the time of writing, the cost of constructing the base 32-channel HF-1 hardware, including parts, PCB fabrication, and assembly, would be approximately $10,000 (USD). The approximate cost breakdown for the HF-1 hardware is listed in Table 5.

2.3. Data recording and real-time processing examples

At the time of writing, the HF-1 system has been used by six different laboratory groups at the MGH/HST Martinos Center for Biomedical Imaging (Charlestown, MA) and the Naval Submarine Medical Research Laboratory (Groton, CT) in over 100 recording

Table 5
Cost breakdown for HF-1 hardware

Item	Cost
32 channel external amplifier unit	$1,000
Double shielded amplifier cable	$1,200
data acquisition and optical USB units	$7,000
Battery pack	$150
Optical USB cable	$200
National Instruments USB-6210	$700
Total	$10,250

sessions during a period of approximately 3 years. In this paper we will report data from 52 study subjects recorded over this time period. Applications have included auditory and somatosensory EEG/fMRI, visual evoked intracranial recordings in non-human primates during fMRI, EEG/fMRI studies during sleep and general anesthesia, and EEG recordings within a hyperbaric chamber. Recordings during MRI were performed within Siemens 7 T, 3 T (Trio), and 1.5 T (Sonata) scanners (Siemens, Erlangen, German). Recordings during 7 T fMRI, as well as some 3 T recordings, were performed using an 32-channel EEG cap whose leads were constructed from a resistive carbon silver ink-based flexible circuit to prevent RF heating and improve both image and EEG quality, which we will refer to below as the "Ink Cap" (Vasios et al., 2006). Table 2 shows the number of studies performed according to study type. All human studies were conducted with the approval of the Human Research Committee at the Massachusetts General Hospital (for auditory, somatosensory, sleep, and general anesthesia studies), and by the Institutional Review Board at the Naval Medical Submarine Laboratory (hyperbaric chamber recordings). All animal recordings (non-human primates) were conducted with the approval of the Subcommittee on Research Animal Care at the Massachusetts General Hospital. A description of each of the studies is provided below, with example data presented in Section 3.

2.3.1. Real-time visual evoked potentials (VEPs, outside scanner)

VEPs were recorded outside the scanner to test the function of the time-domain real-time event-related potential averaging module. The study subject was presented a full-field flickering checkerboard with inter-stimulus interval of 500 ms, alternating between 15 s of stimulus and 15 s of fixation and rest. Electrodes were placed at O1 and O2, referenced to M1, and recorded at 978 Hz, with amplitude epoch rejection limits set to $\pm 100\,\mu V$ in the real-time averaging module. One study subject was studied under this paradigm.

2.3.2. Alpha wave recordings (7, 3, and 1.5 T)

Alpha waves were recorded by asking a study subject to lay quietly in the static field with eyes closed. Recordings at 7 and 3 T were made using the HF-1 system, sampling at 978 Hz with 32 channels. Recordings at 7 T used the 32-channel Ink Cap (Vasios et al., 2006) with medium-impedance leads (~ 2 to $5\,k\Omega$ distributed across lead), while recordings at 3 T used either the same cap, a high-impedance version of that cap (~ 20 to $30\,k\Omega$ distributed across lead), or an 8-channel electrode set constructed with low impedance carbon fibers (see Section 2.3.3 for details). Alpha waves were also recorded at 1.5 T using a 32-channel OptiLink/SynAmps recording system (Compumedics Neuroscan, Charlotte, NC) with a 32-channel MRI compatible Quickcap (Compumedics Neuroscan, Charlotte, NC) modified to employ a bipolar montage to reduce ballistocardiogram noise. The 1.5 T data were previously reported in (Bonmassar et al., 2002). Alpha waves were recorded in 9 subjects at 7 T, 13 subjects at 3 T, and 6 subjects at 1.5 T.

2.3.3. Radio frequency (RF) interference testing (3 T)

The RF attenuation of the shielding enclosure was demonstrated by comparing localizer (3 T, 10 mm slice thickness, 0.55 mm in-plane resolution, 512×512 matrix, TE = 5 ms, TR = 20 ms, 40° flip angle) and functional images (4 mm slice thickness, 1 mm skip, $3.1\,mm \times 3.1\,mm$ in-plane resolution, 64×64 matrix, coronal orientation, TE = 30 ms, TR = 9 s, 90° flip angle) with the shielding chassis in place and then removed. The localizer was chosen for comparison because it is empirically more sensitive to RF noise from the instrument than other sequences. One study subject was studied with shielding chassis removed, while the remainder of

3 T measurements with shielding in place were drawn from the auditory studies described below.

2.3.4. Auditory EEG/fMRI (3 and 7 T)

Subjects were presented one of two types of auditory stimuli to elicit either the 40-Hz auditory steady state response (ASSR) or the midlatency auditory evoked potential (MLAEP). For the ASSR, study subjects were presented with 30 s trains of 12.5 ms noise bursts at 40-Hz, in a 30-s stimulus ON, 30 s stimulus OFF pattern over a 15 min run (both at 7 and 3 T). For MLAEP, subjects were presented 100 ms 1/3-octave pink-noise bursts with a center-frequency of 1 kHz and an inter-stimulus interval of 2 s, arranged in a 30 s ON/OFF block paradigm (7 T only). Stimuli were delivered using a laptop running Presentation (Neurobehavioral Systems, Inc., Albany, CA) with an Echo Indigo 24-bit PCMCIA audio card (Echo Digital Audio Corporation, Carpinteria, CA) and Koss ESP-950 electrostatic headphones retrofitted by our group for MRI-compatibility (Koss Corporation, Milwaukee, WI) or MR Confon Optime 1 headphones (MR Confon, Madeburg, Germany). Recordings at 3 T were made using an 8-channel bipolar montage (M2 → T8, T8 → C6, C6 → C4, C4 → Cz, Cz → C3, C3 → C5, C5 → T7 and T7 → M1), with leads constructed from low impedance carbon fibers (Marktek FiberOhm, 7 Ω/in., $\sim 150\,\Omega$ total; Marktek Inc., Chesterfield, MI), while recordings at 7 T were performed using the 32-channel Ink Cap (Vasios et al., 2006) with medium-impedance leads (~ 2–$5\,k\Omega$ distributed across lead), at a sampling rate of 978 Hz in both cases. Functional MRI acquisitions were arranged according to a "long TR" auditory fMRI design, with 15-slice volume acquisition in 1 s followed by an 8–9 s silent period (at 3 T: 4 mm slice thickness, 1 mm skip, $3.1\,mm \times 3.1\,mm$ in-plane resolution, 64×64 matrix, coronal orientation, TE = 30, 90° flip angle, with cardiac gating to achieve TR of ~ 9 s; at 7 T: 3.1 mm slice thickness, 1.15 mm skip, TE = 20, TR = 10 s, without cardiac gating). This long TR arrangement allows hemodynamic responses elicited by acoustic scanner noise to subside before the next volume acquisition (Hall et al., 1999, 2000). Structural MRI at 3 and 7 T were acquired using a T1-weighted MPRAGE sequence (1.3 mm thick, $1.3\,mm \times 1\,mm$ in-plane resolution, TR/TE = 2530/3.3 ms, 7° flip angle). A total of 21 subjects were studied using the ASSR paradigm, 8 at 7 T and 13 at 3 T. One study subject was studied with MLAEP at 7 T.

ASSRs were computed in the frequency domain using multi-taper spectral analysis (Percival and Walden, 1993) from 4-s EEG windows $x_n(t)$ (M1 → Cz) centered 4-s prior to each volume acquisition (Fig. 7). This arrangement reflects the observation that the BOLD hemodynamic delay from stimulus onset is approximately 4-s (Hall et al., 1999; Hall et al., 2000). For each window, the EEG was linearly detrended and power spectra were computed and averaged separately for stimulus ON and OFF conditions using the multi-taper method (Percival and Walden, 1993), with time-bandwidth product NW = 4:

$$\bar{P}_{ON}(\omega) = \frac{1}{N_{ON}} \sum_{n \in \{Stimulus\,ON\}} P(\omega, n),$$
$$\bar{P}_{OFF}(\omega) = \frac{1}{N_{OFF}} \sum_{n \in \{Stimulus\,OFF\}} P(\omega, n), \tag{1}$$

where $P(\omega, n)$ represents the power spectral estimate corresponding to the nth EPI volume, and N_{ON} and N_{OFF} represent the number of EEG windows corresponding to stimulus ON and stimulus OFF conditions, respectively. In cases where EEG windows overlapped the transition from ON to OFF or vice versa, the window was assigned to the condition with the majority of overlap with the window. To summarize the 40-Hz response over the entire recording run, the
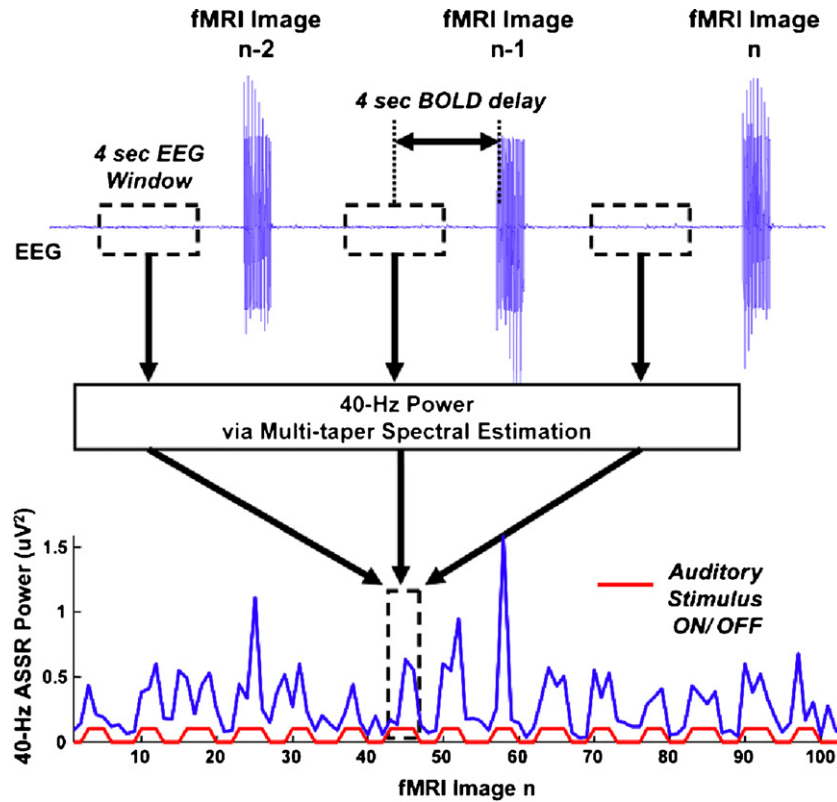
Fig. 7. Overview of ASSR acquisition and analysis during EEG/fMRI.

power ratio $S(\omega)$ was computed:

$$S(\omega) = \frac{\bar{P}_{ON}(\omega)}{\bar{P}_{OFF}(\omega)}. \tag{2}$$

To represent temporal variations in the ASSR, the 40-Hz amplitude (square-root of power) time series was computed $a(n) = \sqrt{P(\omega, n)}|_{\omega=40\,Hz}$. This amplitude time-series was then used as a regressor in an fMRI time-series model with polynomial drift
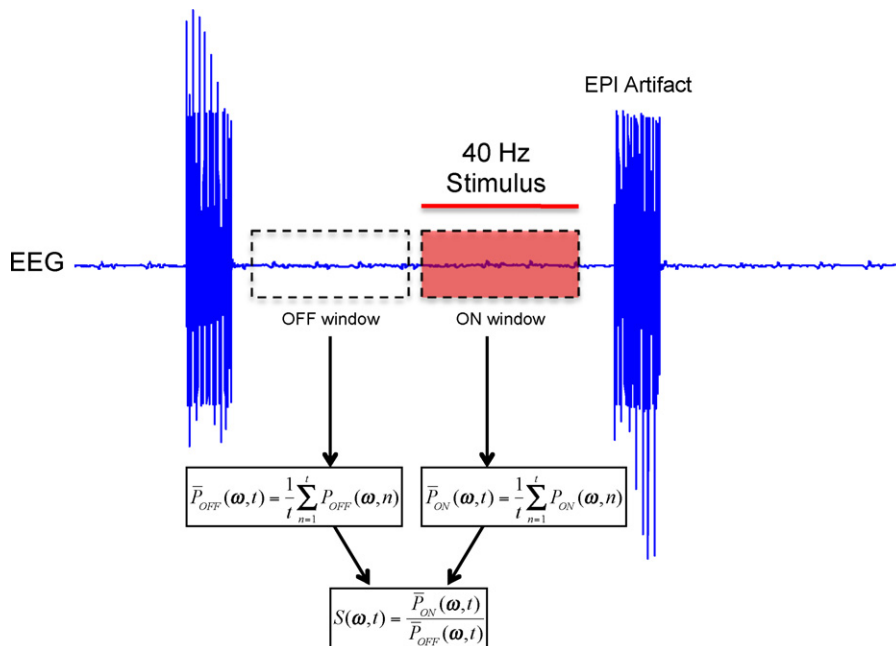

Fig. 8. Overview of ASSR acquisition and analysis during real-time EEG/fMRI.

terms and an ON/OFF indicator function convolved with a gamma-function, fitted using the program "3dDeconvolve" in the AFNI software package (Cox, 1996).

2.4. Real-time auditory EEG-fMRI (3 T)

Real-time 40-Hz ASSR were acquired at 3 T using a long-TR design with a fixed 10-s TR (10 coronal slices, 4 mm thick, 1 mm skip, 3.1 mm × 3.1 mm in-plane resolution, 64 × 64 matrix, TE = 30, 90° flip angle, volume acquisition time of 626 ms). A 4-s train of 40-Hz noise bursts was presented in the second half of each silent interval, cycled in 30 s ON/OFF blocks. Two study subjects were studied under this paradigm, with EEG recorded from Cz and Fz, referenced to M1, at 978 Hz in each subject, and in a separate session using the high-impedance version of the 32-channel "Ink Cap" in one of the subjects. The real-time EEG processing module was configured to segment windows of EEG data containing this 4-s stimulus, with a 4-s pre-stimulus baseline (Fig. 8). With each stimulus, the running average of the power spectra was updated, and the power ratio was updated as well:

$$\bar{P}_{ON}(\omega, t) = \frac{1}{t} \sum_{n=1}^{t} P_{ON}(\omega, n) = \left(\frac{t-1}{t}\right) \bar{P}_{ON}(\omega, t) + \left(\frac{1}{t}\right) P_{ON}(\omega, n)$$

$$\bar{P}_{OFF}(\omega, t) = \frac{1}{t} \sum_{n=1}^{t} P_{OFF}(\omega, n) = \left(\frac{t-1}{t}\right) \bar{P}_{OFF}(\omega, t) + \left(\frac{1}{t}\right) P_{OFF}(\omega, n)$$

$$S(\omega, t) = \frac{\bar{P}_{ON}(\omega, t)}{\bar{P}_{OFF}(\omega, t)}$$

(3)

Each EEG data window was linearly detrended, and the power spectrum was estimated using the periodogram (Percival and Walden, 1993), chosen for its computational simplicity. At the same time, real-time fMRI activation maps were computed using the Neuro3D feature of the Siemens Numaris 4 Syngo MR B15 MRI acquisition program (Siemens, Erlangen, Germany).

2.4.1. Intracranial visual evoked potentials in non-human primates

Intracranial visual evoked potentials were measured in non-human primate (*Macaca mulatta*) during fMRI in a head-only 3 T MRI scanner (Siemens Allegra,; Siemens, Erlangen, Germany). Twenty-six Teflon coated platinum-iridium microwires (25 μm diameter, 90% platinum, 10% iridium from California Fine Wire Company, Grover Beach, CA) were manually inserted normal to the cortical surface to depths of 2–6 mm, along the rostral bank of the arcuate sulcus. Each wire tip was beveled and stripped of ~40 μm of Teflon coating prior to insertion, giving a total surface of ~3600 μm². Measured impedances of the electrodes were between 34 and 61 kΩ (at 100 Hz). An external impedance buffer was constructed to provide a 5 kΩ input impedance to the HF-1 amplifiers. Gradient echo T2*-weighted echo planar images (50 coronal slices, 64 × 64 in-plane matrix, TR = 3 s, TE = 25 ms, 1.25 mm × 1.25 mm × 1.25 mm voxels, flip angle = 90°) were acquired with a single saddle-shaped, radial transmit-receive surface coil (12 cm diameter) positioned over the monkey's head. To minimize the effect of gradient artifacts on the intracranial potential recordings, 3 s fMRI scans were interleaved with 3 s silent periods. The visual stimulus consisted of a full screen (16°) radial checkerboard flicker, presented for 500 ms. To reliably record visual evoked potentials, the study subject was trained on a visual fixation task, and eye position was monitored at 120 Hz using an infrared pupil/corneal reflection tracking system (RK-726PCI, Iscan Inc., Burlington, MA). Criteria performance was defined as greater

than 90% within a 2° × 2° window. Visual stimuli were projected at 1024 × 768 resolution and 60 Hz refresh rate, from a LCD projector onto a translucent screen 52 cm from the animals' eyes. A total of 100 responses were used to create an averaged waveform. Because the results of these experiments will be presented in other publications focused on neuroscience, in this paper we will show only the evoked potential data, and corresponding gradient-echo T2* images (without activation maps) to demonstrate the capabilities of the HF-1 system. A total of two subjects, one featuring three sessions, another with one session, were studied under this paradigm.

2.4.2. Sleep studies (3 T)

Study subjects were asked to sleep inside the MRI scanner during EEG and fMRI measurements. Subjects were allowed to adapt to sleeping in the MRI scanner during two prior sessions, one in a "mock" scanner, and another in a real MRI scanner. Scanning was conducted with an interleaved sequence, with volume acquisition in 2 s, followed by a 4-s silent period (35 slices, 3 mm × 3 mm × 3.5 mm, oriented parallel to the AC-PC, TR = 2 s, TE = 30 ms, flip angle = 90°). Ballistocardiogram artifacts were removed from the EEG using Kalman adaptive filtering with a motion sensor reference signal (Bonmassar et al., 2002) EEG (M1 → Cz, M1 → Oz) were used to observe sleep-related EEG patterns for sleep scoring. Because the results of these experiments will be presented in other publications focused on clinical medicine and neuroscience, in this paper we will show only the EEG data collected during sleep inside the MRI to demonstrate the capabilities of the HF-1 system. A total of seven subjects were studied under this paradigm.

2.4.3. General anesthesia studies (3 T)

General anesthesia was induced with the drug propofol in healthy post-laryngectomy patient volunteers. The study subjects' airways were secured using cuffed tracheostomy tubes prior to induction to provide ventilation support for subject safety, and to maintain a stable CO_2 levels to prevent CO_2-induced changes in cerebral blood flow. Hospital standards for off-site administration of general anesthesia were strictly followed, and at least two anesthesiologists, plus a third ACLS-certified person, were present at every study. Study subjects were imaged using the cardiac-gated EEG/fMRI paradigm for 40-Hz ASSR described earlier in Section 2.3.2 at baseline and during induction of general anesthesia. Propofol was administered at effect-site target concentrations of 1.0, 2.0, 3.0, and 4.0 μg/ml using the computer program STANPUMP (Shafer and Gregg, 1992) with a Harvard 22 Infusion Pump (Harvard Apparatus, Holliston, MA). Because the results of these experiments will be presented in other publications focused on clinical medicine and neuroscience, in this paper we will show only a subset of the ASSR and fMRI data to demonstrate the capabilities of the HF-1 system. A total of eight subjects were studied under this paradigm.

2.4.4. Hyperbaric studies

The HF-1 acquisition system was placed inside a hyperbaric chamber and USB and SYNC signals were sent through a penetration panel in order to acquire data from outside the chamber. The 40-Hz auditory stimuli described in Section 2.3.2 were delivered to study subjects during EEG recording with HF-1 at normal pressure, 190 feet (~6 atmospheres pressure), and again at normal pressure, in order to observe electrophysiological effects of hyperbaric nitrogen narcosis. Recordings were limited to safe exposure times described in the United States Navy Diving Manual (United States Dept. of the Navy, 1985). The study subject was in a seated position within the hyperbaric chamber during these studies, and auditory stimuli

were delivered through a loudspeaker. A total of five subjects were studied under this paradigm.

3. Results: performance examples and dissemination

3.1. Hardware distribution

Fig. 9 shows a montage of hardware distribution images for the HF-1 system. Fig. 9A shows the schematic for the digital portion of the data acquisition unit (MCU and USB Interface) in Orcad format. This schematic is linked to the print circuit board (PCB) layout (Fig. 9B), also in Orcad format. The PCB design is double-sided, with eight layers and 5-mil traces, laid out to minimize transmission of RF fields that could interfere with MRI. Fig. 9C shows the fully assembled circuit board for the analog input portion of the data acquisition unit, illustrating the compactness of the PCB, achieved through careful layout and use of surface mount components down to 0402 footprint size. Fig. 9D shows the fully assembled HF-1 data acquisition unit with cover removed, illustrating use of copper-clad Kapton internal shielding to further reduce RF transmission. PCB Gerber files, a complete bill of materials (BOM) with data sheets for all components, automated pick-and-place assembly files, and test procedure files are also included in the hardware distribution (not shown). Fig. 10 shows the fully assembled HF-1 hardware system with all components.

3.2. VEP (outside scanner), alpha wave (3 T), and RF noise recordings (3 T)

Fig. 5 shows a detailed view of a screenshot of the time-domain real-time ERP averaging during a VEP experiment after 120 averages. Fig. 10 shows a comparison of alpha waves recorded at 1.5 T using an Optilink/Synamps + QuickCap setup, compared with alpha waves recorded at 3 T using an HF-1 + high impedance Ink Cap setup. The 1.5 T data shows large ballistocardiogram (BCG) artifacts that obscure the alpha waves, while the HF-1 + high impedance Ink Cap recording shows clear alpha waves, without BCG artifacts. Fig. 12 (panel A) shows an example of alpha waves recorded in the 7 T static field after motion sensor-based adaptive filtering (Bonmassar et al., 2002). Fig. 11 illustrates the effectiveness of the shielding enclosure. During one recording session, the cover to the ADC chassis was removed during imaging (middle column of Fig. 11), resulting in poor image quality compared to images acquired without simultaneous EEG (left column of Fig. 11). In a separate imaging session, with the shielding in place, image noise levels are at nominal levels (right column of Fig. 11).

3.3. Auditory EEG/fMRI at 7 T

Fig. 12 shows examples of auditory EEG/fMRI recorded at 7 T using the HF-1 system. The middle panel (Fig. 12B) shows an exam-
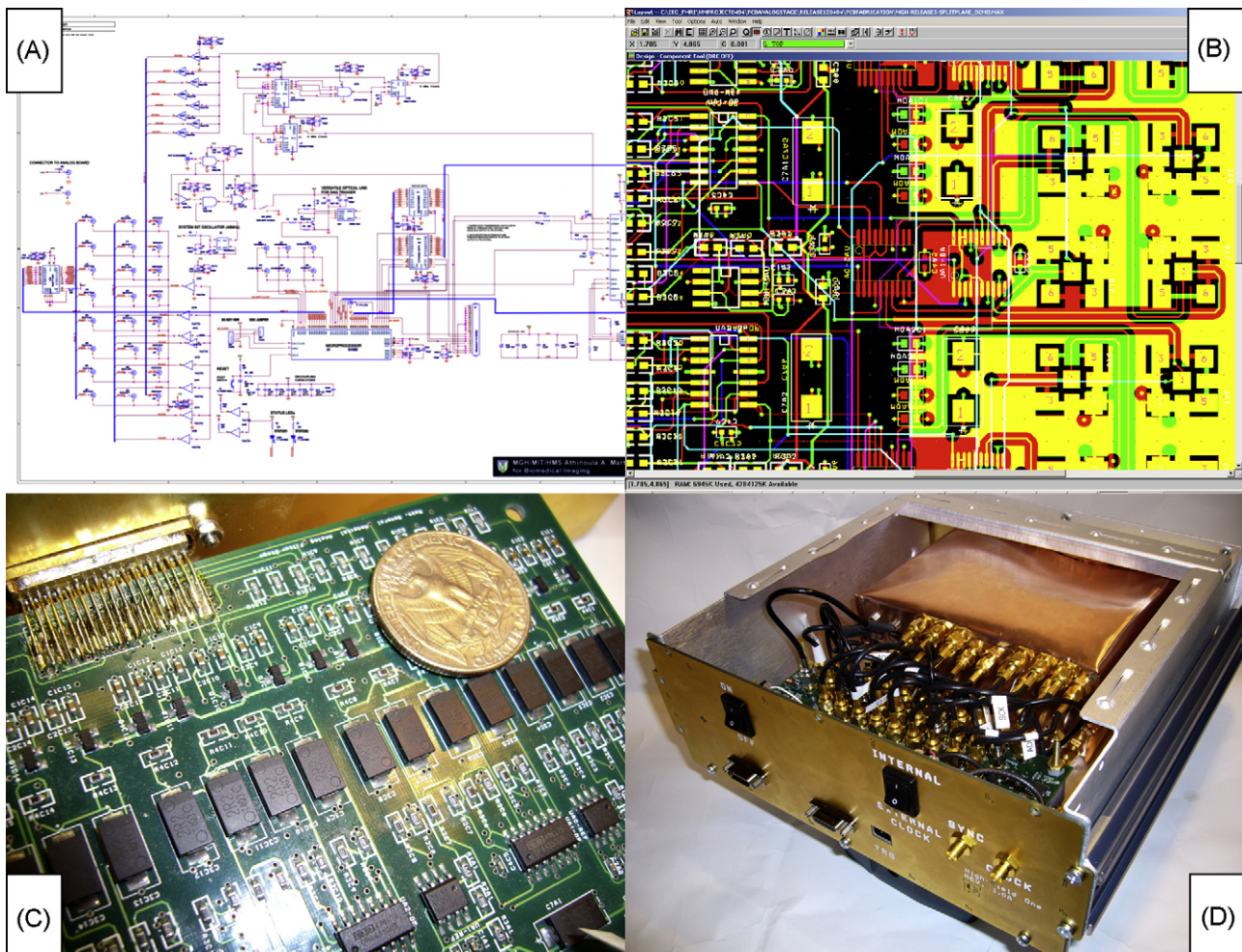

Fig. 9. Examples of HF-1 hardware distribution: (A) circuit schematics, (B) print circuit board layout, (C) completed A/D conversion board and (D) interior of assembled HF-1 data acquisition unit.
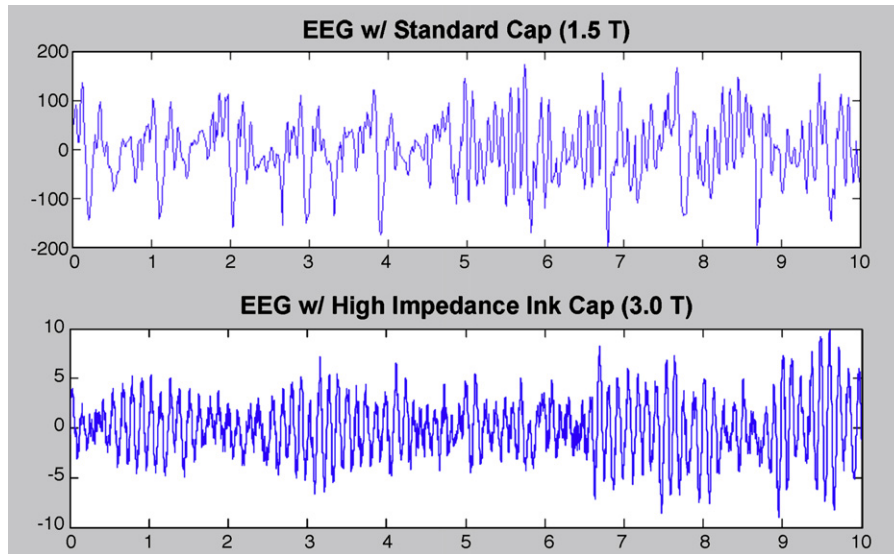
Fig. 10. Comparison of human alpha waves recorded at 1.5 T using Optilink/Synaps + QuickCap system (top), and alpha waves recorded at 3 T using HF-1 + high impedance Ink Cap (bottom).

ple of an auditory evoked potential (AEP, left) recorded during interleaved fMRI at 7 T (right). The activation map (left) is shown overlaid on the gradient echo functional image to illustrate the absence of RF-noise artifacts on the 7 T functional images. The lower panel (Fig. 12C) shows an example of a 40 Hz auditory steady-state response (ASSR, left), shown as a ratio of power spectra comparing stimulus ON versus stimulus OFF periods, also recorded with interleaved fMRI at 7 T (right). Fig. 13 shows an example of the fMRI time series fit in the auditory cortex during 7 T EEG/fMRI when the ASSR amplitude is included as covariate in the fMRI regression model, showing a good correspondence between model fit and temporal fluctuations in the fMRI signal ($P = 0.0145$ for partial F-test for inclusion of ASSR amplitude term in time series model). In Figs. 12 and 13,

one can observe the "central brightening effect" seen in 7 T MRI, due to the dielectric properties of tissues and a resonance effect observed at 300 MHz when using birdcage head coils (Vaughan et al., 2001; Wiggins et al., 2005).

3.4. Real-time auditory EEG/fMRI at 3 T

Figs. 14 and 15 show real-time processing of ASSR during fMRI at 3 T. The top panel of Fig. 14 shows a screen shot of the real-time ASSR (RT-ASSR) module. The left side of the RT-ASSR display shows the most recent update of the ASSR power ratio estimate, in this case showing the results after 19 stimulus presentation epochs (approximately 6 min). The right side of the RT-ASSR dis-
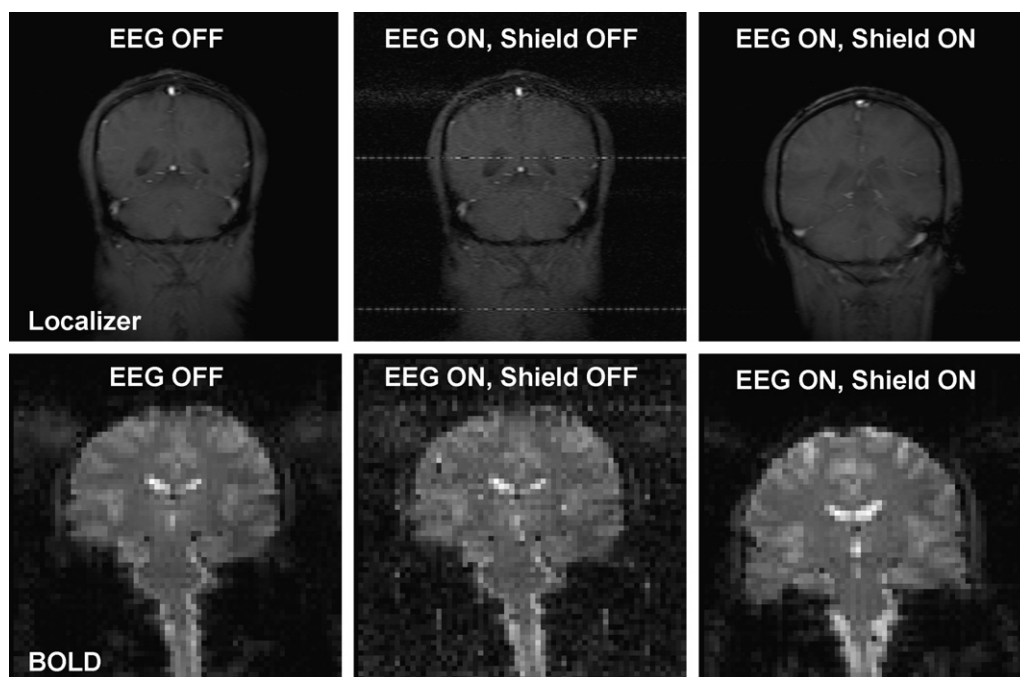
Fig. 11. Effectiveness of RF shielding system for HF-1 amplifier and data acquisition units (3 T). Images taken without shielding (middle column) show a drastic reduction in image quality compared to normal MR images (left column) due to noise from digital processes within the data acquisition unit. When the shielding enclosure is in place, the background noise returns to nominal levels (right column).
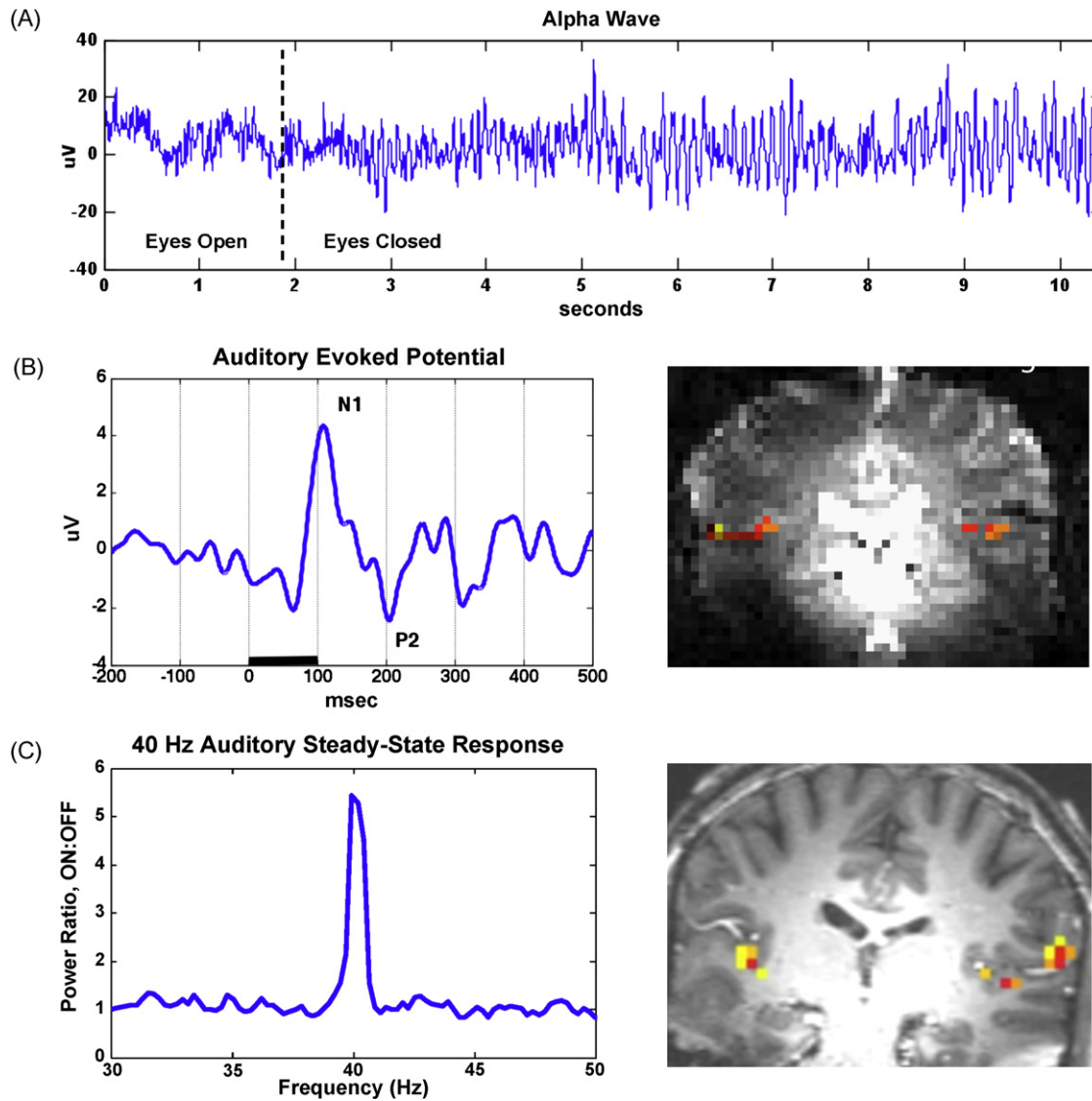
Fig. 12. Examples of human EEG and fMRI recorded at 7 T using the HF-1 system: (A) alpha waves recorded in the 7 T static field after motion sensor-based adaptive filtering (Bonmassar et al., 2002); (B) auditory evoked potentials (AEP, left), recorded during interleaved fMRI at 7 T (right), with the functional map overlaid on the raw gradient echo image to illustrate the absence of RF-noise artifacts; (C) 40 Hz auditory steady-state responses (ASSR, left) also recorded with interleaved fMRI at 7 T (right).
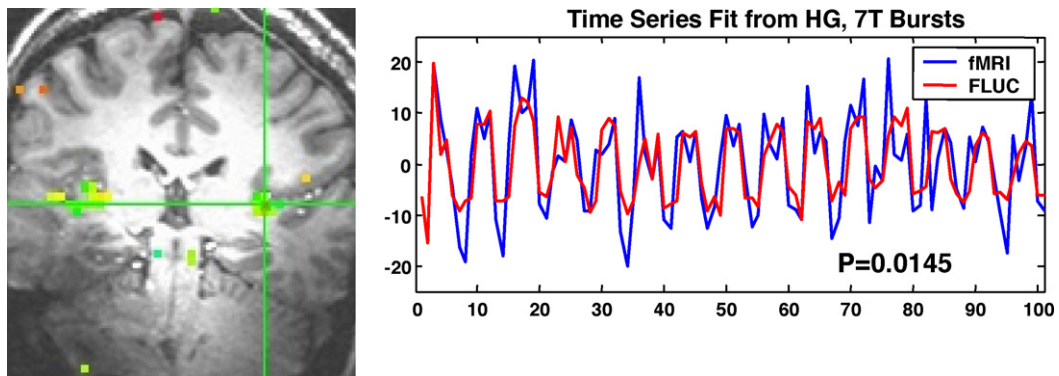

Fig. 13. Example of time-varying ASSR during fMRI in humans at 7 T. The BOLD time series from a single voxel denoted by the crosshairs is show in blue ("fMRI"), while the time series fit employing time-varying fluctuations in the ASSR is shown in red ("FLUC").
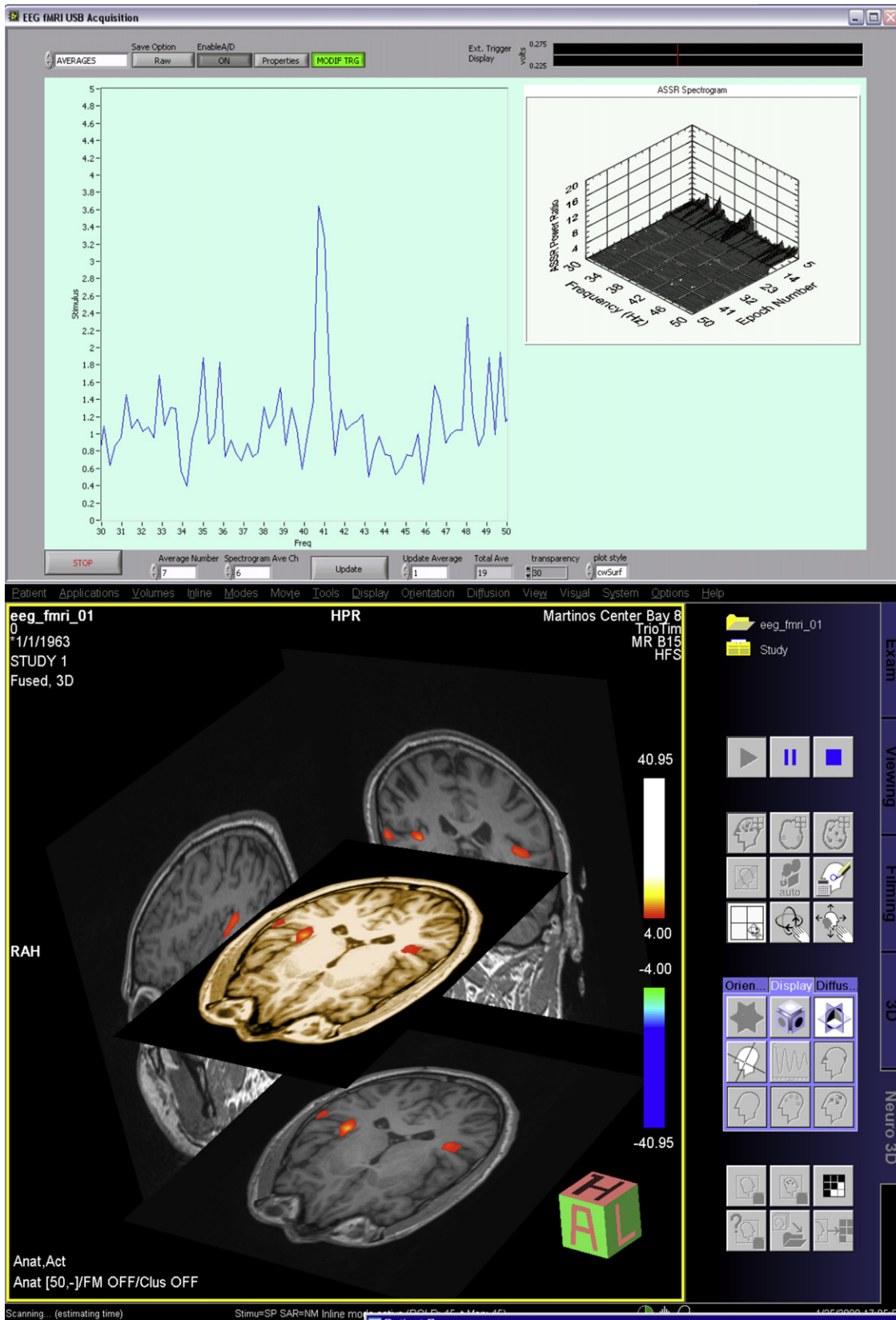
Fig. 14. Example of real-time ASSR during fMRI in humans at 3 T, showing real-time ASSR averaging module (top), and simultaneously acquired real-time fMRI activation maps using Siemens Syngo MR Neuro3D function (bottom).
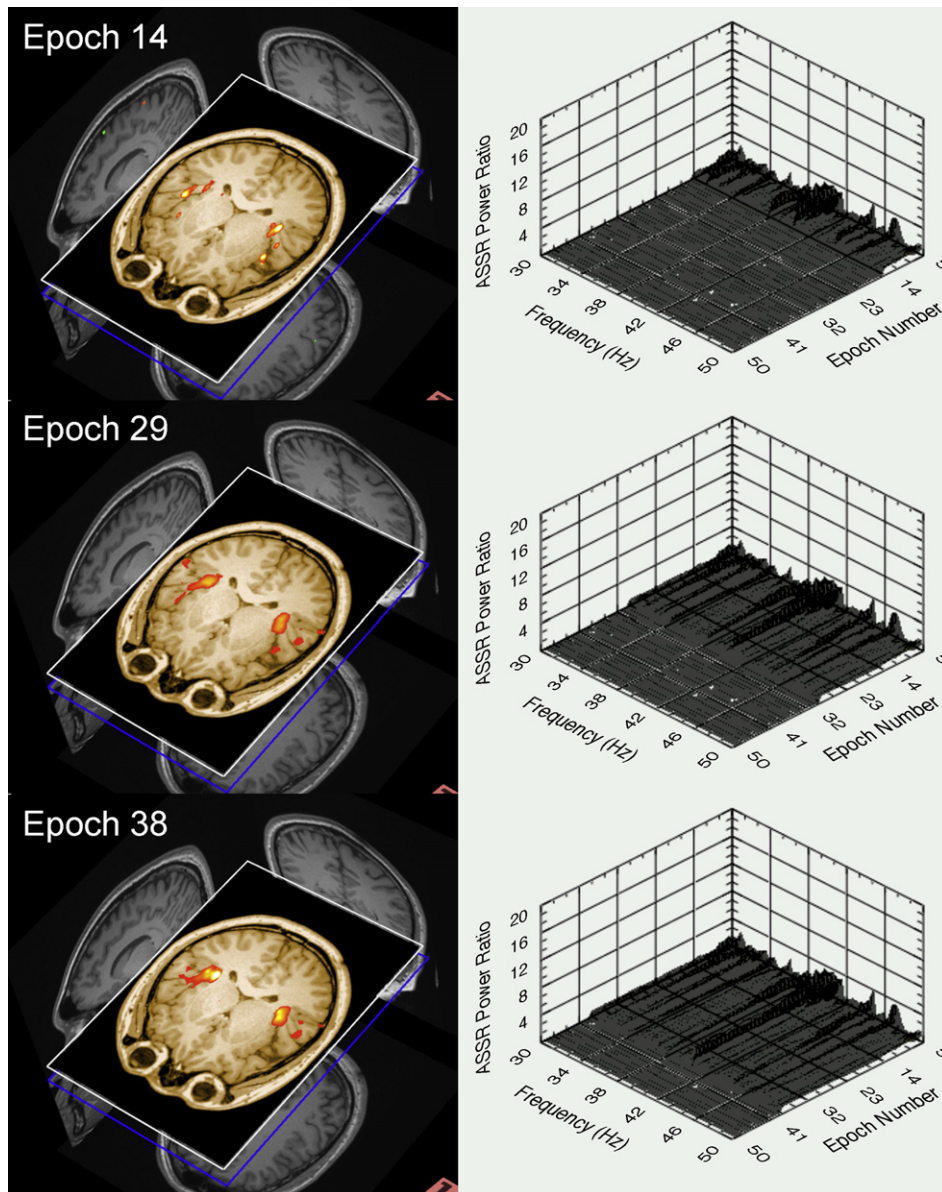
Fig. 15. Evolution of real-time EEG/fMRI data in humans at 3 T, with fMRI activation maps (left), and detail of the real-time ASSR running history (right).

play shows the running history of ASSR power ratio updates in a 3D plot. The RT-ASSR module can work on all EEG channels simultaneously, and includes options for online amplitude-based artifact rejection as well as lowpass, bandpass, or highpass filtering (not shown). A time-domain averaging module is also included with the HF-1 distribution for real-time processing of time-domain ERPs (Fig. 5, showing VEPs). The bottom panel shows a screen shot of real-time fMRI activation maps produced by the Neuro3D feature of the Siemens Numaris 4 Syngo MR B15 MRI acquisition program, acquired at approximately the same time as the RT-ASSR. In Fig. 15, we show several snapshots as time progresses during the same ASSR/fMRI study in a different study subject, with fMRI on the left, and a close-up of the RT-ASSR running history display on the right.

3.5. Intracranial visual evoked potentials in non-human primates

Fig. 16 shows intracranial visual evoked potentials (iVEP) in non-human primates obtained from averaging 100 trials, comparing results obtained outside the scanner (left) and inside the scanner (middle). The initial positive and negative waves of the iVEPs show a similar morphology both outside and inside the scanner. Gradient echo functional images (right) obtained during electrophysiological recording are free of RF-related artifacts.

3.6. Sleep studies

Fig. 17 shows alpha wave (top) and slow-wave (bottom) EEG patterns obtained during natural sleep during interleaved fMRI. Ballistocardiogram artifacts were removed using adaptive filtering (Bonmassar et al., 2002). During the first two seconds, the imaging (gradient) artifact can be observed, with a rapid recovery facilitated by HF-1's DC frequency response. The slow-wave EEG pattern shows a characteristic high-amplitude, low frequency pattern, also facilitated by the DC frequency response of the system. The alpha oscillations show a characteristic 8 to 12 Hz frequency and lower amplitude. These EEG recordings were used for sleep scoring.
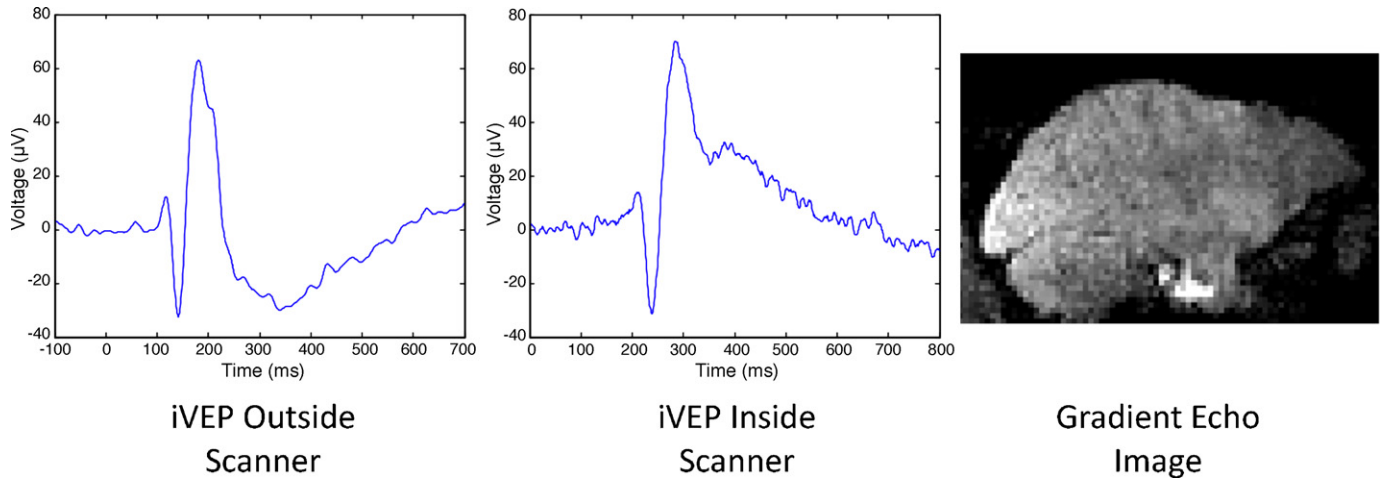
Fig. 16. Example of intracranial VEPs (iVEPs) recorded from non-human primates at 3 T, comparing iVEPs recorded outside (left) and inside the scanner (middle), with gradient echo MR image illustrating lack of RF-related artifacts.

3.7. Anesthesia studies

Fig. 18 shows ASSR and fMRI data from a study subject who received propofol anesthesia. Compared to baseline, the ASSR decreases at the 1 μg/ml target concentration level, and disappears at the 2 μg/ml level. Meanwhile, at 2 μg/ml, where the subject is unconscious (bottom right), fMRI activity in primary auditory cortex persists (middle right), suggesting that auditory processing is preserved after loss of consciousness.

3.8. Hyperbaric physiology

Fig. 19 shows the ASSR power ratio at the baseline state (top), at 190 feet below sea level (fsw) (middle), and after recovery to normal pressure (bottom). At 190 fsw, the 40-Hz response is greatly attenuated compared to baseline and recovery to normal pressure. During these recordings, the HF-1 acquisition system was

exposed to extreme pressures (∼6 atmospheres), high rates of pressure change (5 atmospheres in ∼ 3 min), as well as large temperature changes (room temperature to 40 °C in ∼3 min). SNR and noise level of the instrument was assessed in a different experiment where the instrument was placed in a hyperbaric instrument chamber, and SNR and noise level did not change in a significant way.

4. Discussion

The HF-1 system is an open-source hardware and software system for acquisition and real-time processing of electrophysiology during fMRI. The open-source aspect of this system allows end-users to develop and customize all aspects of hardware and software to suite their specific application. The open-source nature of the HF-1 hardware is particularly important for MRI-related applications, as it provides researchers with a data acquisition hard-
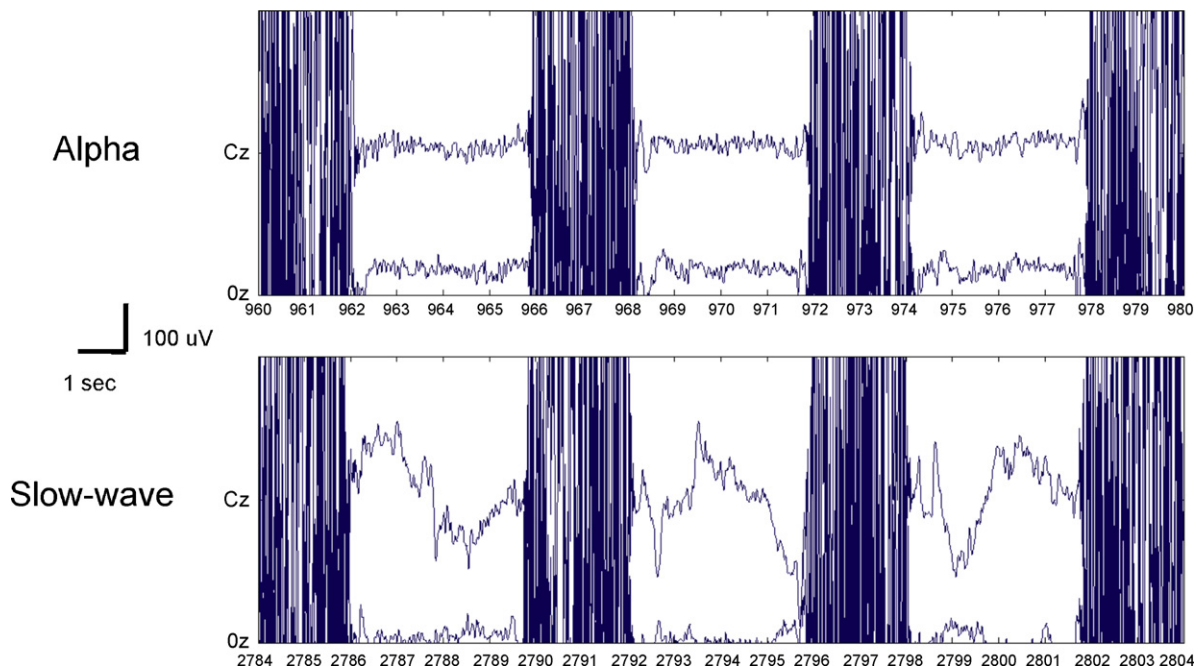

Fig. 17. EEG recorded during fMRI and sleep in humans at 3 T, showing alpha wave (top) and slow-wave (bottom) sleep patterns.
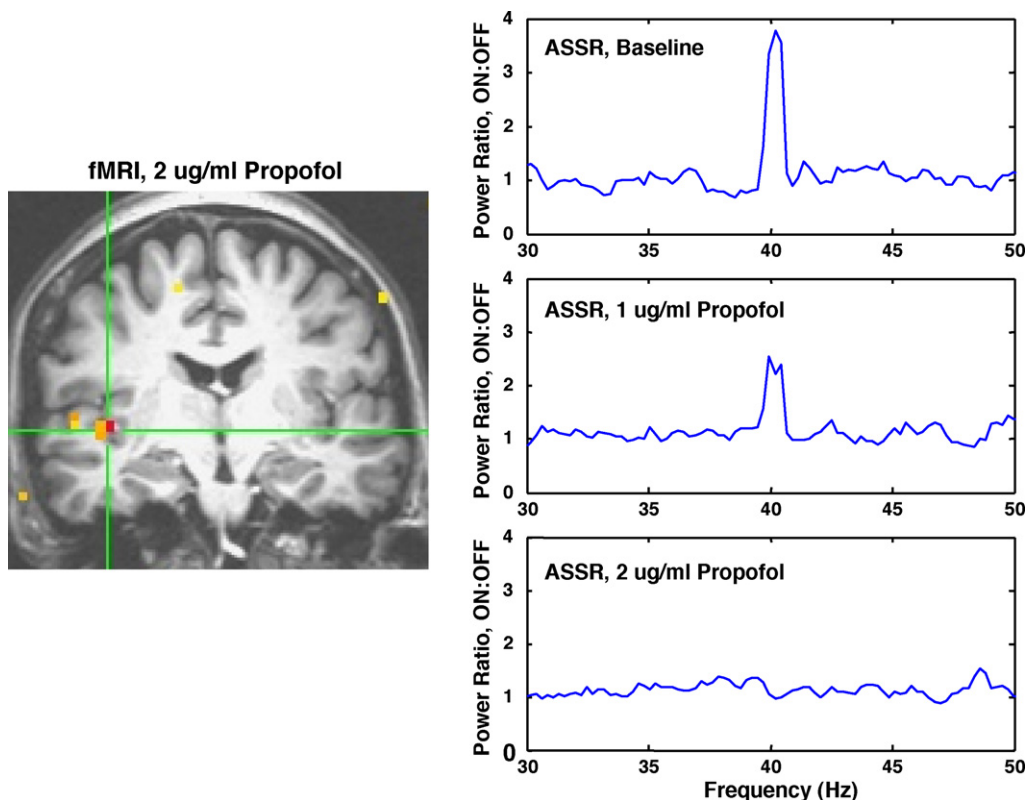
Fig. 18. fMRI (left) and ASSR (left) recorded during induction of general anesthesia in humans at 3 T using propofol.

ware template that meets the stringent and costly requirements of MRI-safety and compatibility as well as electromagnetic compliance. The integrated software subsystems are user-customizable at all levels of organization, from low-level MCU firmware to high-level data acquisition and analysis software. The HF-1 open-source software allows end users to rapidly develop customized real-time acquisition and processing applications. Within neuroscience and clinical medicine there is a growing need for such real-time acquisition and processing solutions, for applications including epilepsy, neurofeedback, sleep studies, and electrophysiological drug studies.

Hardware for simultaneous EEG and fMRI have been developed independently in numerous laboratories (Allen et al., 1998; Garreffa et al., 2004; Goldman et al., 2000; Mirsattari et al., 2005), and are also available commercially from a number of manufacturers such as BrainProducts (Munich, Germany) or Neuroscan-Compumedics (El Paso, Texas). Hardware for electrophysiological recordings during fMRI in animals has also been developed (Logothetis et al., 2001). However, none of these systems provide a complete open-source solution integrating MRI-compatible hardware with user-customizable real-time software. The OpenEEG Project, http://openeeg.sourceforge.net/doc/, is an open-source EEG hardware system that provides an avenue for low-cost EEG acquisition. The OpenEEG system lacks the MRI-specific design features, the specifications and files for automated hardware assembly, and the degree of software integration found in HF-1. Stand-alone systems and software for real-time processing of EEG/fMRI have also been reported in the literature (Garreffa et al., 2003; Mirsattari et al., 2005). Compared with other data acquisition and real-time processing software, the HF-1 software has the advantage that it has been developed within the user-friendly LabView graphical programming environment, facilitating rapid development of real-time signal processing modules, as well as data acquisition and

display modules that can be completely customized to the end-user's specific needs.

A basic use for real-time signal processing is to assess whether or not an adequate amount of data have been recorded during a particular experiment. For simultaneous ERP/fMRI studies, real-time ERP averaging can be used to examine ERP signal quality to ensure that enough ERP epochs have been recorded. Sources of poor signal quality include subject level of arousal, subject movement, and electrode impedance, for instance, all of which can be difficult to detect during a study. Examining ERP results in real-time can help investigators detect and debug problems immediately, resulting in a tremendous savings of time and effort, not to mention peace of mind. For sleep, anesthesia, or resting-state EEG/fMRI studies, which often examine the spectral content of EEG signals as a variable of interest, real-time analysis of frequency spectra could be useful in monitoring the study subject's state. In this paper, we have illustrated both real-time ERP averaging and frequency-domain analyses with real-time 40-Hz ASSR calculations.

Beyond ERP averaging and spectral analysis, one can imagine many new and important applications for real-time processing of electrophysiology during fMRI. For epilepsy studies, a real-time spike detection module could be used to determine whether a sufficient number of interictal spikes have been observed during an experiment. Similarly, a real-time sleep scoring module could be used to ensure that adequate amounts of data are being recorded during each desired stage of sleep. Numerous automatic sleep scoring systems have been proposed (Analog, 2004; Anderer et al., 2005; Atamer et al., 2002; Callini et al., 2000; Chang et al., 1988; Heiss et al., 2002; Holzmann et al., 1999; Korpinen et al., 1994; Penzel and Conradt, 2000; Principe et al., 1989; Principe and Smith, 1985, 1986; Ray et al., 1986; Schwaibold et al., 2002) and many are commercially available, but have yet to be developed for simultaneous electrophysiology during fMRI. EEG-based neurofeedback
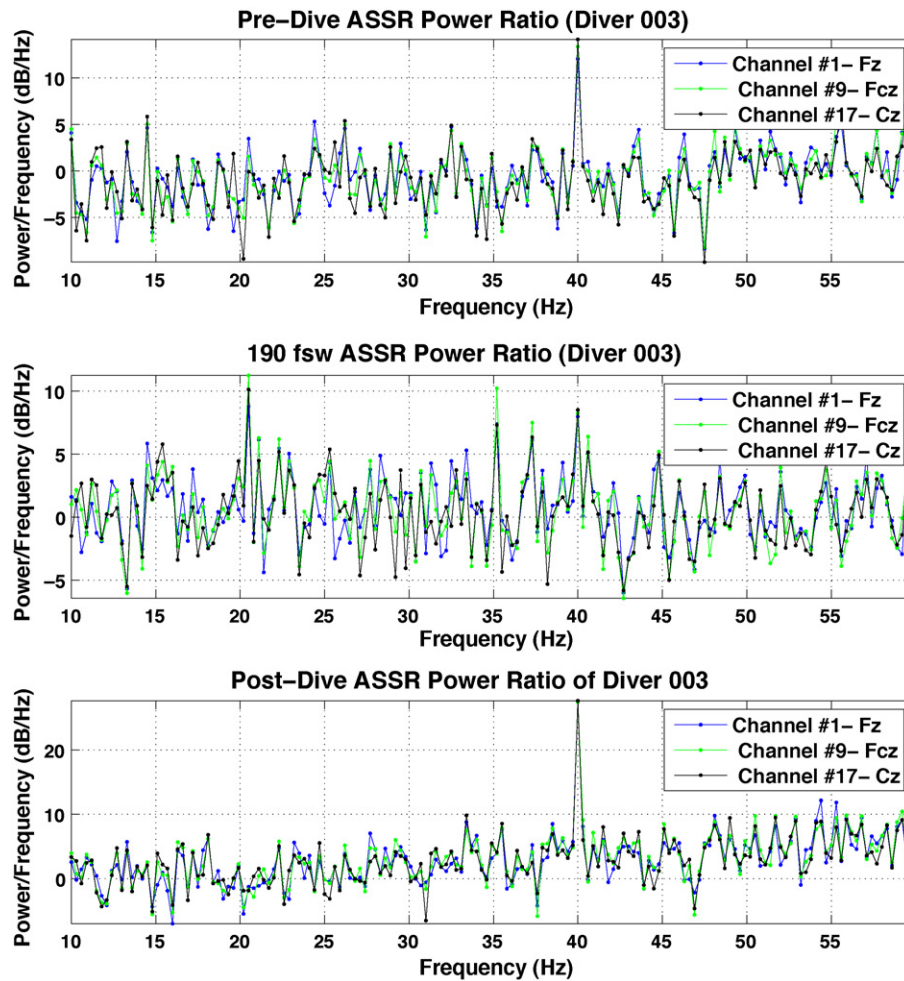
Fig. 19. 40 Hz ASSR during hyperbaric study (non-MRI, Earth's magnetic field), comparing baseline (top), 190 feet below sea level (middle), and recovery to sea level (bottom). Note the ASSR power ratio in this figure is plotted on a log scale.

during fMRI is another application for real-time processing. Neurofeedback is a technique where study subjects are taught how to modulate, through their own will, neural signals derived from EEG that are presented to the subject in real-time either visually or aurally (e.g., screen showing cursor position related to EEG signal features). This technique is becoming a widely used tool in neuroscience and clinical research, and by its very nature requires real-time signal processing (Basmajian, 1981; Delorme and Makeig, 2003; Fox, 1979; Herrmann et al., 2004; Hill and Raab, 2005; Riddle and Baker, 2005; Sinkjaer et al., 2003). Real-time processing of electrophysiological signals for neurofeedback during fMRI would provide the means to correlate neurofeedback with simultaneously observed fMRI and identify neural systems involved in neurofeedback. Numerous drugs with sites of action in the central nervous system produce dose-dependent changes in EEG, including general anesthetics (Rampil, 1998), sedative hypnotics (Veselis et al., 1991), opioid analgesics (Scott et al., 1985), and antidepressants (Dumont et al., 2005). With real-time EEG processing during fMRI, drug levels could be titrated to specific EEG-based endpoints, to allow a systematic investigation of brain function at specific drug-induced electrophysiological states. Outside the MRI environment, HF-1's flexible open-source real-time processing and data acquisition could provide a means to implement variable-rate sampling or compression of electrophysiological data in the neurological intensive care unit (NeuroICU). In the NeuroICU, multi-day recordings can generate terabytes of data at the high sampling rates required to observe rare but important high-frequency bursting activity. With variable rate sampling or compression, temporal resolution could be changed in real-time as dictated by the data. The HF-1 open-source system has been designed to provide a flexible starting point to rapidly develop real-time processing solutions for a wide range of studies such as these.

Open-source dissemination of hardware and software developed from public funding helps fulfill the mandate of publicly funded medical research by making tools freely available to the research community and by providing building blocks for future collaborative development. Open-source dissemination of software has enjoyed a long and fruitful history, and such developments within the neuroscience community have made a tremendous impact. Open-source dissemination of hardware has been slower to develop, largely because of the relatively greater difficulty associated with constructing hardware devices compared to installing or modifying software code. However, resources for rapid construction of electronic devices have become readily available. For instance, companies offering services to build PCBs, place and solder components, and test assembled devices can be contracted for a modest fee in most locales or via the internet. The HF-1 system takes advantage of these resources by providing detailed construction files that allow the system to be constructed in a largely automated fashion using such services. In the near term, the increasing availability of such resources will make open-source hardware developments such as HF-1 accessible to many research

laboratories. In the longer term, the ongoing development of self-contained electronic fabrication laboratories (e.g., "FAB LAB," http://fab.cba.mit.edu/ (Mikhak et al., 2002)) will allow researchers with even very modest resources to take advantage of open-source hardware.

5. Conclusions

The HF-1 open-source hardware and software system presented here is a fully functional integrated hardware and software system for electrophysiological recordings during MRI. This open-source system provides the building blocks for custom MRI-compatible data acquisition hardware, as well as custom data acquisition and real-time signal processing tools that can be rapidly developed within the LabView environment. This is a unique project in that this distribution provides not only open-source software and hardware schematics, but also detailed construction and manufacturing specifications to help end-users build their own system for electrophysiology during MRI with high accuracy and low cost. This system has been used by multiple research groups on applications including studies of auditory, somatosensory, and visual systems, real-time EEG/fMRI, clinical studies including sleep, anesthesia, and hyperbaric physiology, and intracranial recordings from animals.

Acknowledgements

Appendix A

See Table A.1.

Table A.1
List of acronyms

ADC	Analog to digital converter/conversion
ASSR	Auditory steady state response
BOM	Bill of materials
CO_2	Carbon dioxide
DAQ	Data acquisition
DC	Direct current
DDS	Direct digital synthesis
EEG	Electroencephalogram
EMI	Electromagnetic interference
ERP	Event-related potential
fMRI	Functional magnetic resonance imaging
fsw	Feet below sea level
G	Gain on external amplifier unit
HF-1	High-field one
iVEP	Intracranial visual evoked potentials
LCD	Liquid crystal display
LFP	Local field potentials
LSB	Least-significant bit
MCU	Microcontroller unit
mil	1/1000th of an inch
MLAEP	Midlatency auditory evoked potential
MPRAGE	Structural MRI sequence
MRI	Magnetic resonance imaging
MUA	Multi-unit activity
NeuroICU	Neurological intensive care unit
PCB	Print circuit board
PCMCIA	laptop card bus
PCO_2	Partial pressure of carbon dioxide
RC	Resistor–capacitor circuit
RF	Radio frequency
RMS	Root-mean-squared
RT	Real-time
SNR	Signal to noise
SYNC	Synchronization
T	Tesla
T1	Longitudinal magnetization time constant used in MRI
T2*	Transverse relaxation time constant used in MRI
TE	Echo time, MRI parameter
TR	Repetition time, MRI parameter
µg/ml	Micrograms per milliliter
USB	Universal serial bus
VEP	Visual evoked potential

References

Allen PJ, Josephs O, Turner R. A method for removing imaging artifact from continuous EEG recorded during functional MRI. Neuroimage 2000;12:230–9.

Allen PJ, Polizzi G, Krakow K, Fish DR, Lemieux L. Identification of EEG events in the MR scanner: the problem of pulse artifact and a method for its subtraction. Neuroimage 1998;8:229–39.

Analog D. AD620: low cost low power instrumentation amplifier, revision G. Analog Devices: Norwood, MA; 2004.

Anami K, Mori T, Tanaka F, Kawagoe Y, Okamoto J, Yarita M, et al. Stepping stone sampling for retrieving artifact-free electroencephalogram during functional magnetic resonance imaging. Neuroimage 2003;19:281–95.

Anderer P, Gruber G, Parapatics S, Woertz M, Miazhynskaia T, Klosch G, et al. An E-health solution for automatic sleep classification according to Rechtschaffen and Kales: validation study of the Somnolyzer 24 × 7 utilizing the Siesta database. Neuropsychobiology 2005;51:115–33.

Angelone LM, Potthast A, Segonne F, Iwaki S, Belliveau JW, Bonmassar G. Metallic electrodes and leads in simultaneous EEG-MRI: specific absorption rate (SAR) simulation studies. Bioelectromagnetics 2004;25:285–95.

Angelone LM, Vasios CE, Wiggins G, Purdon PL, Bonmassar G. On the effect of resistive EEG electrodes and leads during 7 Tesla MRI: simulation and temperature measurement studies. Magn Reson Imaging 2006;24:801–12.

Atamer A, Delaney M, Young LR. An expert system for fault management assistance on a space sleep experiment. Arch Ital Biol 2002;140:303–13.

Basmajian JV. Biofeedback in rehabilitation: a review of principles and practices. Arch Phys Med Rehabil 1981;62:469–75.

Bonmassar G, Hadjikhani N, Ives JR, Hinton D, Belliveau JW. Influence of EEG electrodes on the BOLD fMRI signal. Hum Brain Mapp 2001;14:108–15.

Bonmassar G, Purdon PL, Jaaskelainen IP, Chiappa K, Solo V, Brown EN, et al. Motion and ballistocardiogram artifact removal for interleaved recording of EEG and EPs during MRI. Neuroimage 2002;16:1127–41.

Callini G, Essig SM, Heher DM, Young LR. Effectiveness of an expert system for astronaut assistance on a sleep experiment. Aviat Space Environ Med 2000;71:1023–32.

Chalamala BR, Temple D. Big and bendable. IEEE Spectrum 2005;42:50–6.

Chang TG, Smith JR, Principe JC. An expert system for multichannel sleep EEG/EOG signal analysis. Biomed Sci Instrum 1988;24:19–25.

Chen DW. Boy, 6, dies of skull injury during M.R.I. The New York Times; 2001.

Cox RW. AFNI: software for analysis and visualization of functional magnetic resonance neuroimages. Comput Biomed Res 1996;29:162–73.

Delorme A, Makeig S. EEG changes accompanying learned regulation of 12-Hz EEG activity. IEEE Trans Neural Syst Rehabil Eng 2003;11:133–7.

Dumont GJ, de Visser SJ, Cohen AF, van Gerven JM. Biomarkers for the effects of selective serotonin reuptake inhibitors (SSRIs) in healthy subjects. Br J Clin Pharmacol 2005;59:495–510.

Fox CD. Feedback control of hemispheric EEG alpha. Percept Mot Skills 1979;48:147–55.

Garreffa G, Bianciardi M, Hagberg GE, Macaluso E, Marciani MG, Maraviglia B, et al. Simultaneous EEG-fMRI acquisition: how far is it from being a standardized technique? Magn Reson Imaging 2004;22:1445–55.

Garreffa G, Carni M, Gualniera G, Ricci GB, Bozzao L, De Carli D, et al. Real-time MR artifacts filtering during continuous EEG/fMRI acquisition. Magn Reson Imaging 2003;21:1175–89.

Goldman RI, Stern JM, Engel Jr J, Cohen MS. Acquiring simultaneous EEG and functional MRI. Clin Neurophysiol 2000;111:1974–80.

Hall DA, Haggard MP, Akeroyd MA, Palmer AR, Summerfield AQ, Elliott MR, et al. "Sparse" temporal sampling in auditory fMRI. Hum Brain Mapp 1999;7:213–23.

Hall DA, Summerfield AQ, Goncalves MS, Foster JR, Palmer AR, Bowtell RW. Time-course of the auditory BOLD response to scanner noise. Magn Reson Med 2000;43:601–6.

Heiss JE, Held CM, Estevez PA, Perez CA, Holzmann CA, Perez JP. Classification of sleep stages in infants: a neuro fuzzy approach. IEEE Eng Med Biol Magn 2002;21:147–51.

Herrmann BL, Wessendorf TE, Ajaj W, Kahlke S, Teschler H, Mann K. Effects of octreotide on sleep apnoea and tongue volume (magnetic resonance imaging) in patients with acromegaly. Eur J Endocrinol 2004;151:309–15.

Hill H, Raab M. Analyzing a complex visuomotor tracking task with brain-electrical event related potentials. Hum Mov Sci 2005;24:1–30.

Holzmann CA, Perez CA, Held CM, San Martin M, Pizarro F, Perez JP, et al. Expert-system classification of sleep/waking states in infants. Med Biol Eng Comput 1999;37:466–76.

Huang-Hellinger FR, Breiter HC, McCormack G, Cohen MS, Kwong KK, Sutton JP, et al. Simultaneous functional magnetic resonance imaging and electrophysiological recording. Hum Brain Mapp 1995;3:13–23.

Instruments T. ADS1254: 24-bit, 20 kHz, low power analog-to-digital converter. Texas Instruments, Inc.: Dallas, TX; 2001.

Ives JR, Warach S, Schmitt F, Edelman RR, Schomer DL. Monitoring the patient's EEG during echo planar MRI. Electroencephalogr Clin Neurophysiol 1993;87:417–20.

Korpinen L, Partinen M, Telakivi T, Martikainen K, Pietila T, Peltola J, et al. Evaluation of Sleep Expert—a computer-aided decision support system for sleep disorders. Med Inform (Lond) 1994;19:247–52.

Lemieux L, Allen PJ, Franconi F, Symms MR, Fish DR. Recording of EEG during fMRI experiments: patient safety. Magn Reson Med 1997;38:943–52.

Lemieux L, Salek-Haddadi A, Josephs O, Allen P, Toms N, Scott C, et al. Event-related fMRI with simultaneous and continuous EEG: description of the method and initial case report. Neuroimage 2001;14:780–7.

Logothetis NK, Pauls J, Augath M, Trinath T, Oeltermann A. Neurophysiological investigation of the basis of the fMRI signal. Nature 2001;412:150–7.

Mandelkow H, Halder P, Boesiger P, Brandeis D. Synchronization facilitates removal of MRI artefacts from concurrent EEG recordings and increases usable bandwidth. Neuroimage 2006;32:1120–6.

Mei J, Lovell MR, Mickle MH. Formulation and processing of novel conductive solution inks in continuous inkjet printing of 3-D electric circuits. IEEE Trans Electron Packaging Manuf 2005;28:857–69.

Mikhak B, Lyon C, Gorton T, Gershenfeld N, McEnnis C, Taylor J. FAB LAB: an alternate model of ICT for development. In: 2nd international conference on open collaborative design for sustainable innovation; 2002.

Mirsattari SM, Ives JR, Bihari F, Leung LS, Menon RS, Bartha R. Real-time display of artifact-free electroencephalography during functional magnetic resonance imaging and magnetic resonance spectroscopy in an animal model of epilepsy. Magn Reson Med 2005;53:456–64.

Niazy RK, Beckmann CF, Iannetti GD, Brady JM, Smith SM. Removal of FMRI environment artifacts from EEG data using optimal basis sets. Neuroimage 2005;28:720–37.

Penzel T, Conradt R. Computer based sleep recording and analysis. Sleep Med Rev 2000;4:131–48.

Percival DB, Walden AT. Spectral analysis for physical applications. New York: Cambridge University Press; 1993.

Portas CM, Krakow K, Allen P, Josephs O, Armony JL, Frith CD. Auditory processing across the sleep-wake cycle: simultaneous EEG and fMRI monitoring in humans. Neuron 2000;28:991–9.

Principe JC, Gala SK, Chang TG. Sleep staging automaton based on the theory of evidence. IEEE Trans Biomed Eng 1989;36:503–9.

Principe JC, Smith JR. Automatic recognition of spike and wave bursts. Electroencephalogr Clin Neurophysiol Suppl 1985;37:115–32.

Principe JC, Smith JR. SAMICOS—a sleep analyzing microcomputer system. IEEE Trans Biomed Eng 1986;33:935–41.

Rampil IJ. A primer for EEG signal processing in anesthesia. Anesthesiology 1998;89:980–1002.

Ray SR, Lee WD, Morgan CD, Airth-Kindree W. Computer sleep stage scoring—an expert system approach. Int J Biomed Comput 1986;19:43–61.

Riddle CN, Baker SN. Manipulation of peripheral neural feedback loops alters human corticomuscular coherence. J Physiol 2005;566:625–39.

Schomer DL, Bonmassar G, Lazeyras F, Seeck M, Blum A, Anami K, et al. EEG-linked functional magnetic resonance imaging in epilepsy and cognitive neurophysiology. J Clin Neurophysiol 2000;17:43–58.

Schwaibold M, Schochlin J, Bolz A. Automated sleep stage detection with a classical and a neural learning algorithm–methodological aspects. Biomed Technol (Berl) 2002;47(Suppl. 1 Pt 1):318–20.

Scott JC, Ponganis KV, Stanski DR. EEG quantitation of narcotic effect: the comparative pharmacodynamics of fentanyl and alfentanil. Anesthesiology 1985;62:234–41.

Shafer SL, Gregg KM. Algorithms to rapidly achieve and maintain stable drug concentrations at the site of drug effect with a computer-controlled infusion pump. J Pharmacokinet Biopharm 1992;20:147–69.

Sinkjaer T, Haugland M, Inmann A, Hansen M, Nielsen KD. Biopotentials as command and feedback signals in functional electrical stimulation systems. Med Eng Phys 2003;25:29–40.

United States Food and Drug Administration CfDaRH. A primer on medical device interactions with magnetic resonance imaging systems; 1997.

United States Dept. of the Navy. US Navy diving manual, revision 1, 1 June 1985 ed. Navy Dept.: Washington, DC; 1985.

Vasios CE, Angelone LM, Purdon PL, Ahveninen J, Belliveau JW, Bonmassar G. EEG/(f)MRI measurements at 7 Tesla using a new EEG cap ("InkCap"). Neuroimage 2006;33:1082–92.

Vaughan JT, Garwood M, Collins CM, Liu W, DelaBarre L, Adriany G, et al. 7 T vs. 4 T: RF power, homogeneity, and signal-to-noise comparison in head images. Magn Reson Med 2001;46:24–30.

Veselis RA, Reinsel R, Alagesan R, Heino R, Bedford RF. The EEG as a monitor of midazolam amnesia: changes in power and topography as a function of amnesic state. Anesthesiology 1991;74:866–74.

Wiggins GC, Potthast A, Triantafyllou C, Wiggins CJ, Wald LL. Eight-channel phased array coil and detunable TEM volume coil for 7 T brain imaging. Magn Reson Med 2005;54:235–40.